

## Highlights

### **A passive, blade-mounted ultrasonic bat deterrent for wind turbines**

Zhangming Zeng, Szu-Fu Huang, William N. Alexander, Anupam Sharma

- The deterrent consists of aerodynamic whistles that use cavity resonance to generate ultrasonic tones.
- Wind tunnel measurements verify steady ultrasonic tone production.
- The deterrent works over ranges of flow speeds and blade pitches with an insignificant aerodynamic penalty.
- Numerical simulations reveal the working mechanism to be Rossiter modes.
- The aeroacoustics predictions are verified with the far-field acoustic measurements
- Interactions between adjacent cavities and their impact on radiated ultrasound are investigated numerically.

# A passive, blade-mounted ultrasonic bat deterrent for wind turbines

Zhangming Zeng<sup>a</sup>, Szu-Fu Huang<sup>b</sup>, William N. Alexander<sup>b</sup>, Anupam Sharma<sup>a,\*</sup>

<sup>a</sup>*Department of Aerospace Engineering, Iowa State University, 537 Bissell Road, Ames, 50011, Iowa, USA*

<sup>b</sup>*Department of Aerospace and Ocean Engineering, Blacksburg, 24061, Virginia, USA*

---

## Abstract

A novel aerodynamic-whistle-based ultrasonic tone generator is proposed that has the potential to serve as a bat deterrent when installed on wind turbine rotor blades. The device uses blade-relative flow to excite resonance in cavities that are geometrically tailored to generate tones at the desired ultrasonic frequencies. A comprehensive experimental and numerical study is presented wherein two such deterrent designs are investigated. Experiments are performed in an anechoic wind tunnel where the deterrents are mounted on a blade section with the NACA 0012 profile. Measurements show that the deterrents produce the desired tonal spectrum when the tunnel flow speed exceeds a threshold value. There is also a maximum flow speed above which the deterrents do not generate tones. Variations with flow speed and blade angle of attack are investigated. Acoustic beamforming is used for source localization with partial success.

The compressible unsteady Reynolds-averaged Navier-Stokes equations are solved with the SST  $k-\omega$  turbulence model to simulate the aeroacoustics of the deterrents. Two-dimensional simulations capture the tonal frequencies and the trends with flow speed and blade angle of attack observed in the experiments. Three-dimensional simulations are performed with span-periodic boundaries for two deterrent configurations – one with one resonator modeled and another with two resonators modeled. The flow unsteadiness is higher in the two-resonator configuration; however, the unsteady pressures in the two resonators are nearly out of phase. The Ffowcs Williams-Hawkings acoustic analogy is used to compute the far-field acoustics. The simulations capture the tonal sound pressure levels at the fundamental frequency and the second harmonic.

---

\*Corresponding author; Email: [sharma@iastate.edu](mailto:sharma@iastate.edu)

## 1. Introduction

The US has an installed wind capacity of 140 GW (6% of its total electric supply). The national goal is 40% wind-based electricity, with a projected annual expansion of 66 GW per year over the next decade. This growth will partially be propelled by enhancements in turbine and wind farm design (e.g., [Hu et al. \(2015\)](#); [Rosenberg et al. \(2014\)](#)) that are enabled by novel numerical techniques such as [Chen et al. \(2016\)](#); [Moghadassian et al. \(2016\)](#); [Moghadassian and Sharma \(2018, 2020\)](#); [Rosenberg and Sharma \(2016\)](#). However, achieving this tremendous growth of wind as a truly clean and renewable energy resource requires addressing its adverse ecological impacts, particularly on bats.

Wind energy is one of the largest sources of anthropogenic mortality in bats ([Cryan, 2011](#); [Cryan and Brown, 2007](#)) and is considered one of the largest sources of direct mortality for some bat species ([O’Shea et al., 2016](#)). Estimates of annual turbine-related bat fatalities are in the hundreds of thousands ([Smallwood, 2013](#); [Voigt et al., 2015](#)), and annual bat fatality per wind turbine can be as high as fifty ([Arnett and Baerwald, 2013](#); [Hayes, 2013](#)), although site-to-site variability in fatality rate is quite large. Combined with significant existing environmental risks that bats face, such as White-nose Syndrome, which has led to the death of over 5 million bats in eastern North America since its identification in New York in 2006 ([Zimmerman, 2009](#)), wind-related bat mortality is driving certain species towards extinction ([Cheng et al., 2021](#); [Frick et al., 2020](#); [Friedenberg and Frick, 2021](#)).

Multiple strategies are currently being pursued to mitigate bat fatalities at wind turbines. These strategies encompass: a) operational mitigation ([Arnett et al., 2013](#); [Baerwald et al., 2009](#); [Martin et al., 2017](#)), involving the reduction of power generation at low wind speeds, and b) deterring bats from wind farms using ultrasonic deterrents ([Arnett et al., 2013](#); [Romano et al., 2019](#); [Weaver et al., 2020](#)), ultraviolet lights ([Gorresen et al., 2015](#)), and/or application of textured paints on turbine towers ([Huzzen, 2019](#)). A big drawback of operational mitigation is the reduced energy capture due to power curtailment at low wind speeds, which can render it cost-prohibitive in many circumstances. Therefore, few companies implement this strategy unless mandated by local rules and regulations. In contrast, bat deterrence technologies do not necessitate curtailment and represent an efficient alternative. Initial trials of such deterrents have shown promise ([Arnett et al., 2013](#)); however, their long-term efficacy still requires conclusive validation. Combinations of different technologies, such as curtailment and ultrasonic deterrents, have also been explored ([Good](#)

1 [et al., 2022](#)).

2 Bats navigate and forage using echolocation at ultrasonic frequencies. Consequently, they avoid  
3 regions where their echolocation signals are jammed or overwhelmed by high-amplitude ultrasound.  
4 [Schirmacher \(2020\)](#) showed that the deterrence signal need not be broadband; a tonal spectrum also  
5 provides bat deterrence capability. Compared to broadband, a tonal signal/spectrum concentrates  
6 its acoustic energy into select frequencies, allowing for the augmentation of the intensity of these  
7 tones and enabling a longer range. Also, deterrents that generate a tonal spectrum require less  
8 power and are a plausible choice for “passive” operation. By passive operation, we imply that the  
9 deterrent is driven by blade-relative airflow and does not require any external power source (e.g.,  
10 electricity or compressed air).

11 Currently employed ultrasonic deterrents utilize electromechanical transducer-driven speakers,  
12 as described in [Horn et al. \(2008a\)](#), to produce ultrasound. The Bat Deterrent System (BDS)  
13 developed by NRG Systems ([Schirmacher, 2020](#)) is an example of such a deterrent. One unit of the  
14 NRG BDS consists of six sub-arrays, each generating ultrasonic tones at prescribed frequencies via  
15 multiple transducers. Such a unit can generate tones distributed between 20 kHz to 50 kHz, which  
16 covers the echolocation frequencies of most bat species in the USA. [Schirmacher \(2020\)](#) verified the  
17 six-tone BDS to be effective in reducing bat fatality. In their field study, [Weaver et al. \(2020\)](#) found  
18 that ultrasonic deterrents significantly reduced fatalities in certain bat species.

19 The electromechanical ultrasonic deterrents have the following limitations: a) they rely on exter-  
20 nal power, constraining their possible placement to the turbine nacelle and tower, b) maintenance  
21 challenges arise due to susceptibility to rain/water damage, leading to increased operational costs,  
22 and c) atmospheric absorption prevents the deterrence signal (ultrasound) from reaching the blade  
23 tips, rendering them ineffective in regions with elevated bat fatality risks resulting from high blade  
24 speeds.

25 Aerodynamic ultrasonic deterrents have also been pursued. [Romano et al. \(2019\)](#) tested a device  
26 in which compressed air was accelerated in a converging-diverging nozzle and ejected as a supersonic  
27 jet. The turbulence in the jet shear layer generates broadband noise in the ultrasonic frequency  
28 range (20 – 100 kHz). Aerodynamic whistling, or flow-excited resonance, is an effective way of  
29 generating tonal (ultra)sound. An aerodynamic whistle is a self-sustaining oscillator that generates  
30 high-amplitude acoustic tones ([Chanaud, 1970](#)). The feedback mechanism is the essence of aerody-  
31 namic whistles. Based on the feedback mechanism, [Chanaud \(1970\)](#) classified aerodynamic whistles

1 into three categories. In Class I whistles, the flow instability provides the feedback directly, whereas  
2 the feedback is provided by the sound generator in Class II whistles, and by the resonator/sound  
3 reflector in Class III whistles. Flow-excited resonance is widely observed in nature. A notable  
4 illustration of this occurs when a fluid jet moves through a confined area (hole), similar to how  
5 humans whistle by directing air through the small gap formed by their lips. This produces what  
6 is known as “hole tones,” where the mouth’s cavity functions as a Helmholtz resonator ([Rayleigh,](#)  
7 [1896](#)). Our ability to modify the whistling frequency by altering the shape of the mouth cavity has  
8 been experimentally investigated by [Wilson et al. \(1971\)](#).

9 Flow over a cavity is also a common source of aerodynamically generated sound/noise. Cavity  
10 noise can be classified as either a Class II or a Class III whistle. [Gloerfelt \(2009\)](#) identified the  
11 possible mechanisms of cavity noise to be: (i) Rossiter modes ([Rossiter, 1966](#)), which occur because  
12 of the feedback from the acoustic waves generated when the free shear layer over the cavity interacts  
13 with its downstream edge, (ii) Helmholtz resonance due to the compressibility of the fluid in the  
14 cavity, and (iii) standing-wave resonance in the cavity (depth, longitudinal and spanwise modes).  
15 Rossiter modes are associated with Class II whistles, while Helmholtz resonance and standing-  
16 wave resonance are Class III whistles. Multiple resonance mechanisms co-exist in some cases, e.g.,  
17 Helmholtz resonance can exist simultaneously with standing wave resonance in a cavity ([Bennett](#)  
18 [et al., 2017](#)).

19 While typically used to generate human-audible sound, aerodynamic whistles can be tailored  
20 to generate ultrasound ([Sharma and Zeng, 2023](#)). The advantages of aerodynamic-whistle-based  
21 ultrasonic deterrents include design simplicity (no moving parts), low cost, and the potential for  
22 generating high-amplitude ultrasound with minimal power (in terms of air supply) requirements.

23 In this work, we investigate aerodynamic-whistle-based passive ultrasonic bat deterrents for wind  
24 turbines. These deterrents are intended to be mounted on turbine blades and use the blade-relative  
25 air flow to excite resonance and generate tones at ultrasonic frequencies. In contrast, “active”  
26 aerodynamic whistles require a compressed air supply; we have investigated active aerodynamic  
27 whistles in prior works ([Zeng and Sharma, 2021, 2023, 2025](#)). Besides the ability to operate passively  
28 using blade-relative airflow, another key advantage of blade-mounted deterrents is that they are  
29 located at/near the source of bat fatalities ([Horn et al., 2008b](#); [Kunz et al., 2007](#)), minimizing the  
30 distance the signal (ultrasound) produced by the deterrents has to travel. This is advantageous  
31 because atmospheric absorption heavily attenuates high frequencies. Modern utility-scale wind

1 turbine rotor blades are reaching lengths upward of 120 m. It is nearly impossible for high ultrasonic  
2 frequencies to travel such distances and protect the blade tips from deterrents on the turbine  
3 nacelle/hub.

4 Two passive whistle designs targeting fundamental frequencies 20 kHz and 10 kHz are designed,  
5 prototyped, and investigated. The onset flow speed for cavity oscillations in the resonators is  
6 not known a priori. The 20 kHz resonator, being smaller, is expected to have a higher onset flow  
7 speed (see [Krishnamurty \(1955\)](#)). The 10 kHz design is a risk mitigation measure – to ensure that  
8 resonance is observed in the measurements given the speed limitation of the wind tunnel (described  
9 in Section 3.1).

10 Systematic numerical and experimental analyses are carried out to quantify the acoustic perfor-  
11 mance of the whistles, assess the impact of the whistles on the aerodynamic performance of the blade  
12 section where they are mounted, and identify the sound generation mechanisms. The experiments  
13 are conducted in the Virginia Tech Stability Wind Tunnel in its hemi-anechoic configuration. The  
14 measurements show that the passive whistle deterrent can readily generate the desired frequency  
15 spectrum under typical operating conditions of utility-scale wind turbines. Numerical predictions  
16 of the radiated sound are obtained by coupling the near-field computational fluid dynamics solution  
17 with an acoustic analogy. Based on our experimental and numerical results, the proposed deterrent  
18 design has the potential for future field deployment.

## 19 **2. Passive whistle design**

20 The passive whistle is an adaptation of the active whistle described in [Zeng and Sharma \(2023\)](#).  
21 Figure 1a shows a computer model of the active whistle. In the active whistle, compressed air  
22 is forced into a channel where it passes over two identical resonating chambers facing each other.  
23 [Zeng and Sharma \(2023\)](#) showed that Helmholtz resonance dominates sound generation and the two  
24 resonators oscillate out-of-phase, nearly canceling the sound radiation at the fundamental frequency  
25 ( $f_R$ ) of a single resonator and the odd harmonics ( $3 \times f_R$ ,  $5 \times f_R$ , ...). Sound radiation is therefore  
26 limited to the even harmonics ( $2 \times f_R$ ,  $4 \times f_R$ , ...) of the fundamental frequency.

27 The passive whistle is designed to be embedded into the airfoil (Fig. 1b) or on a sleeve that  
28 can be attached to the airfoil (Fig. 2c). The resonating chamber in the passive whistle is similar to  
29 that in the active whistle, but it is exposed directly to the external flow over the airfoil rather than  
30 being confined to a channel. There is no “opposing” resonator to provide an out-of-phase signal

1 and cancel out the odd harmonics. Since the fundamental tone is not canceled, the geometry of  
 2 the chamber has to be scaled to ensure ultrasonic radiation, i.e., the fundamental frequency of the  
 3 resonator has to be increased to lie in the ultrasonic range. This leads to a reduction in resonator  
 size. The key geometric parameters of the passive whistle are shown in Fig. 1c.

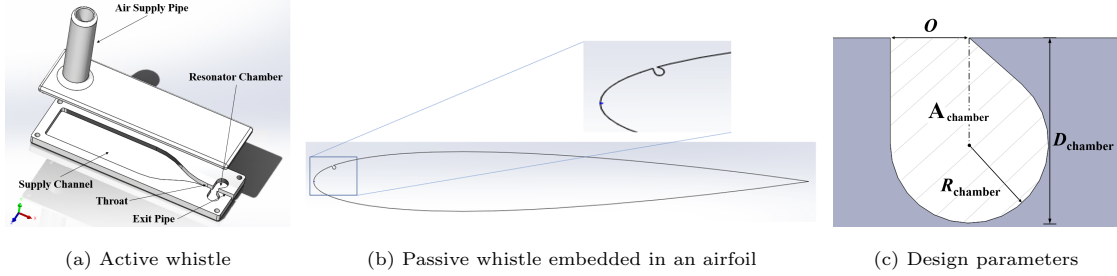


Figure 1: Computer drawings of the active and passive whistle designs: (a) active whistle design of Zeng and Sharma (2023), and (b) the proposed passive whistle embedded in an airfoil near its leading. The geometry of the resonator in the passive whistle is borrowed from the active whistle. The key design parameters of the passive whistle are shown in panel (c);  $A_{\text{chamber}}$  is the area of the resonating chamber.

4

## 5 2.1. Designs for wind tunnel testing

6 Two passive whistle designs are developed for experimental evaluation: (1) a high-frequency  
 7 (HF) design and (2) a low-frequency (LF) design. Table 1 lists the design parameters for the two  
 8 passive whistle configurations and theoretical estimates of their Helmholtz resonance frequencies.  
 9 Note that the fundamental tone of the LF design is in the human-audible frequency range and,  
 10 hence, does not qualify as an ultrasonic whistle/deterrent. The whistles are located at 4% chord  
 11 downstream of the blade leading edge and are oriented such that the openings of the resonating  
 12 chambers are aligned with the local airfoil surface. The deterrent is formed by repeating these  
 13 whistles along the span of the blade (Fig. 2).

14 For the prototypes tested in the Virginia Tech Stability Tunnel (facility description in Sec-  
 15 tion 3.1), the deterrent is engraved on a thin “sleeve” that wraps around the leading edge of the  
 16 blade model. The deterrents can be directly engraved on the blade, but the sleeve approach was  
 17 chosen to allow the testing of multiple deterrents on the same baseline blade model. The drag  
 18 force assists in keeping the sleeve/prototype attached to the blade, which minimizes the risk of  
 19 the prototype tearing off the blade and damaging the wind tunnel. The leading-edge geometry of

Table 1: The design parameters for the two passive whistles that are experimentally evaluated. Theoretical estimates of the Helmholtz resonance frequency ( $f_R$ ) are also listed for each design. Appendix B of Zeng and Sharma (2023) explains how  $f_R$  is estimated.

<i>Configuration</i>	$D_{\text{chamber}}$ [mm]	$R_{\text{chamber}}$ [mm]	$O$ [mm]	$A_{\text{chamber}}$ [mm <sup>2</sup> ]	$f_R$ (kHz)
High frequency (HF)	2.24	0.96	0.96	3.482	29.0
Low frequency (LF)	5.60	2.40	2.40	21.39	11.7

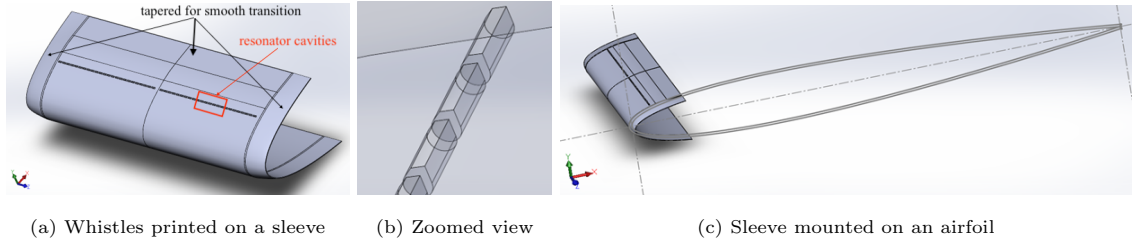


Figure 2: A computer model of the passive deterrent design: (a) whistles engraved on a sleeve, (b) a zoomed view of the resonating cavities (whistles), and (c) the sleeve fitted on the nose of a blade formed by extruding the NACA 0012 airfoil.

1 the sleeve is obtained by normal extrusion of the original airfoil shape with tapering at the edges  
2 to ensure a smooth transition to the baseline blade geometry. Figure 2c demonstrates the sleeve  
3 design and how it fits the blade at the leading edge.

4 For use on existing wind turbine blades, where engraving the deterrents on the blades would be  
5 expensive and risky, and having a sleeve that goes around the leading edge can be costly and might  
6 adversely impact the blade’s aerodynamic performance, the following approach can be taken. The  
7 deterrents can be 3D printed on a small substrate that follows the local blade surface contour, and  
8 the substrate can be glued or fastened to the blade.

9 Figure 3 shows the deterrent prototypes fabricated via 3D printing using acrylic. One row with  
10 48 resonator slots was printed on both sides of the sleeve (corresponding to the suction and pressure  
11 sides of the blade). Each resonating cavity is 5 mm long in the span direction for the HF design and  
12 7 mm long for the LF design, with a 1 mm gap between adjacent cavities. This design approach  
13 was chosen over a single cavity spanning the entire length of the deterrent to prevent spanwise flow  
14 and to avoid additional, low-frequency resonant modes corresponding to standing waves in the span  
15 direction.



1        Figure 3b shows the resonator cavities engraved on the sleeve. The sleeve is designed to fit the  
2        blade model in the Virginia Tech Stability Wind Tunnel (see Fig. 4a). Due to the limitation of the  
3        3D printer, each passive deterrent was printed in four parts (two with resonator slots engraved on  
4        them and two tapered ends), which were later assembled before mounting on the blade model in  
5        the wind tunnel. The 3D printed parts were hand polished using 2000-grit sandpaper for a smooth  
6        surface finish.

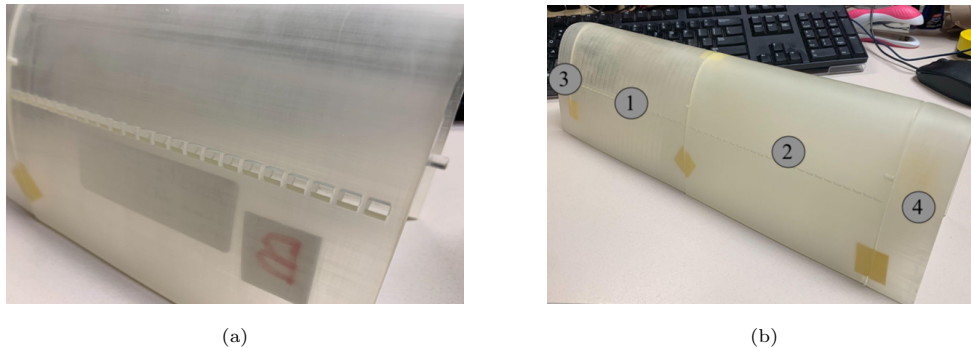


Figure 3: A 3D printed passive deterrent on a sleeve. The deterrent is printed in four parts due to the size limitation of the 3D printer. (a) a zoomed view of the resonating cavities (resonators), and (b) the assembled sleeve with the resonators engraved in it.

### 7    **3. Methods**

#### 8    *3.1. Experimental methodology*

9        Experiments were conducted in the Virginia Tech Stability Wind Tunnel to evaluate the acoustic  
10       performance of the passive deterrents. The wind tunnel has a 1.83 m  $\times$  1.83 m test section and  
11       was set up in its hemi-anechoic configuration (see Fig. 4a). The port wall of the facility is made of  
12       a single layer of tensioned Kevlar fabric backed by an anechoic chamber. The starboard wall is a  
13       flat, non-porous aluminum wall on which the array is mounted. The test section’s floor and ceiling  
14       upstream and downstream of the blade model are acoustically treated. The blade is mounted at  
15       the center of the test section, and the deterrent (marked as “LE Device” in Fig. 4a) is mounted  
16       at the mid span of the blade. The airfoil used in these experiments is two-dimensional, extended  
17       1.83 m from the floor to the ceiling of the test section, and is constructed with fiberglass. The  
18       two-dimensional airfoil follows a nominal NACA 0012 profile with a 914 mm chord length. The

1 Stability Tunnel can operate at freestream speeds up to 80 m/s but was limited to 60 m/s for  
 2 this experiment. The maximum blade tip speed for land-based utility-scale wind turbines has  
 3 historically been limited to be in the range 75 – 80 m/s (Dykes et al., 2014). Hence, a 60 m/s blade  
 4 speed would occur at a normalized radius,  $r/r_{\text{tip}}$  between 0.75 and 0.8 for such a turbine operating  
 5 at its design point.

6 The sound signal generated by the deterrent is measured using a 120-channel high-frequency  
 7 microphone array (Fig. 4b). The array is mounted on the starboard side of the test section in  
 8 individual sockets which hold the microphones behind wire mesh coverings flush with the tunnel  
 9 wall. This array comprises microphones arranged in logarithmic spirals with a maximum aperture  
 10 of 0.5 m. The array employs GRAS 46BD-FV microphones with a frequency response between 5  
 11 kHz to 70 kHz within  $\pm 2$  dB. Szoke et al. (2022) provides a complete description of this array.

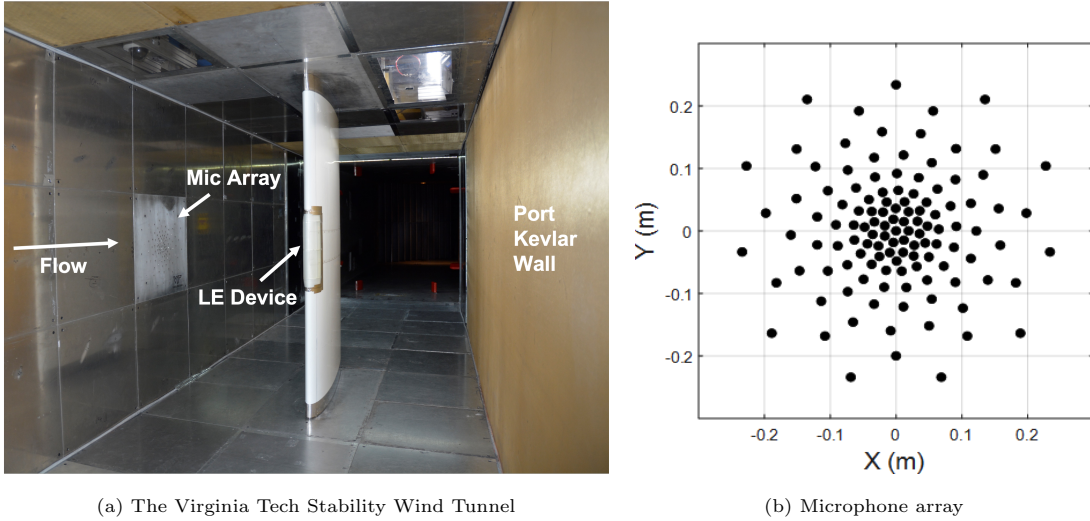


Figure 4: Experimental setup in the Virginia Tech Stability Wind Tunnel. (a) A blade section (extruded NACA 0012 airfoil is used here) is mounted in the middle of the anechoic test section. The passive bat deterrent (labeled ‘LE Device’) is installed on the blade’s leading edge. An array of microphones is mounted flush with the starboard wall to measure the radiated ultrasound and to locate its source via beamforming. The port wall is formed with tensioned Kevlar, which allows the acoustic waves to radiate out while retaining the flow in the tunnel. (b) the 120-channel high-frequency microphone array for measuring radiated ultrasound.

1 *3.2. Measured data processing*

2 Data is acquired for 32 seconds for each microphone in the array at a 374.4 kHz sampling  
3 rate. The cross-spectral matrix is obtained using a signal length of 14,976 samples with a 50%  
4 overlap rate and a Hanning window. Acoustic maps are generated using conventional delay and  
5 sum beamforming with convection and atmospheric attenuation corrections. Integrated spectra  
6 are produced by integrating an area  $0.643 \text{ m} \times 0.592 \text{ m}$  in the streamwise and vertical directions  
7 respectively, centered about the mid-span of the airfoil leading edge. The deterrent is located at a  
8 streamwise distance of 0.0415 m upstream from the center of the microphone array, centered at the  
9 mid-span of the airfoil, and between spanwise locations  $-0.148 \text{ m}$  and  $0.148 \text{ m}$ . The airfoil, lying  
10 along the centerline of the test section, is at a distance of 0.92 m from the plane of the microphone  
11 array.

12 The beamform integrated spectra show multiple equispaced (in frequency) pure tones above the  
13 relatively broad peaks at the harmonics of the resonance frequency of the deterrents (see Fig. 23).  
14 Appendix A presents a plausible explanation for the existence of these unexpected tones. We  
15 hypothesize that these tones are an artifact of measuring sound in the semi-anechoic (as opposed  
16 to fully anechoic) configuration of the wind tunnel; the side wall on which the microphone array is  
17 mounted is an acoustically reflecting surface. To remove these artificial tones, we convolve the data  
18 via a Gaussian filter with a half-width of 150 Hz and present only the filtered results in the paper.

19 *3.3. Numerical methodology*

20 Computational aeroacoustics (CAA) simulations use a two-step process wherein the acoustic  
21 sources are first obtained via unsteady computational fluid dynamics (CFD) simulations. The  
22 radiated acoustic intensity and directivity are subsequently computed via the Ffowcs Williams-  
23 Hawkings acoustic analogy. We use the STAR-CCM+ software for the simulations. The numerical  
24 results supplement the radiating farfield acoustic measurements with near-field flow and acoustics  
25 information to enable a comprehensive understanding of the flow and acoustic mechanisms involved.  
26 The simulations are performed in two and three spatial dimensions. The two-dimensional (2-D)  
27 simulations are used to study the acoustic performance of different resonator sizes at different  
28 freestream flow speeds ( $V_\infty$ ) and angles of attack ( $\alpha$ ). The three-dimensional (3-D) simulations  
29 are used for (a) verification with experiments, (b) investigating the interaction between adjacent  
30 resonators in a deterrent, and (c) predicting the directivity of the radiating acoustic field.

1 Fluid flow is governed by the conservation of mass, momentum, and energy equations. This  
 2 system of equations with an equation of state is called the Navier-Stokes (N-S) equations. We  
 3 solve the unsteady Reynolds-averaged Navier-Stokes (uRANS) equations, obtained by short-time,  
 4 density-weighted (Favre) averaging the Navier-Stokes equations. Favre averaging results in unre-  
 5 solved turbulence (closure) terms, which are modeled using a turbulence closure model. A  $k - \omega$   
 6 turbulence model is used in this work wherein transport equations for the turbulence kinetic energy  
 7 ( $k$ ) and specific dissipation rate ( $\omega$ ) are solved with appropriately tuned production and dissipation  
 8 terms.

9 The density-weighted, short-time averaged N-S equations are

$$\frac{\partial \bar{\rho}}{\partial t} + \frac{\partial}{\partial x_j} (\bar{\rho} \tilde{u}_j) = 0, \quad (1)$$

$$\frac{\partial}{\partial t} (\bar{\rho} \tilde{u}_i) + \frac{\partial}{\partial x_j} (\bar{\rho} \tilde{u}_i \tilde{u}_j) = -\frac{\partial \bar{p}}{\partial x_i} + \frac{\partial}{\partial x_j} (\bar{\tau}_{ij} - \overline{\rho u_i'' u_j''}), \quad (2)$$

$$\frac{\partial}{\partial t} (\bar{\rho} c_p \tilde{T}) + \frac{\partial}{\partial x_j} (\bar{\rho} c_p \tilde{T} \tilde{u}_j) = \frac{\partial \bar{p}}{\partial t} + \tilde{u}_j \frac{\partial \bar{p}}{\partial x_j} + u_j'' \frac{\partial \bar{p}}{\partial x_j} + \frac{\partial}{\partial x_j} \left( \kappa \frac{\partial \tilde{T}}{\partial x_j} + \kappa \frac{\partial \bar{T}''}{\partial x_j} - c_p \overline{\rho u_j'' T''} \right) + \bar{\Phi}, \quad (3)$$

12 where the shear stress term  $\bar{\tau}_{ij}$  can be written as

$$\bar{\tau}_{ij} = \mu \left[ \left( \frac{\partial \tilde{u}_i}{\partial x_j} + \frac{\partial \tilde{u}_j}{\partial x_i} \right) - \frac{2}{3} \delta_{ij} \frac{\partial \tilde{u}_k}{\partial x_k} \right] + \mu \left[ \left( \frac{\partial \bar{u}_i''}{\partial x_j} + \frac{\partial \bar{u}_j''}{\partial x_i} \right) - \frac{2}{3} \delta_{ij} \frac{\partial \bar{u}_k''}{\partial x_k} \right], \quad (4)$$

13 and the dissipation function  $\bar{\Phi}$  can be written as

$$\bar{\Phi} = \overline{\tau_{ij} \frac{\partial u_i}{\partial x_j}} = \bar{\tau}_{ij} \frac{\partial \tilde{u}_i}{\partial x_j} + \tau_{ij} \frac{\partial \bar{u}_i''}{\partial x_j}. \quad (5)$$

14 In the above, the overline ( $\bar{\quad}$ ) denotes short-time-averaging and the tilde ( $\tilde{\quad}$ ) represents density-  
 15 weighted, time-averaging. The superscript ( $''$ ) refers to the fluctuation of the mass-averaged vari-  
 16 ables. To close the system of equations, the Reynolds stress tensor  $-\overline{\rho u_i'' u_j''}$  and some other terms  
 17 (e.g.,  $\partial(\overline{\rho u_j'' T''})/\partial x_j$ ) have to be modeled. In this research, the shear stress transport (SST)  $k - \omega$   
 18 model of [Menter \(1994\)](#) is used.

### 19 3.3.1. Acoustic prediction

20 The Ffowcs Williams-Hawkings (FW-H) acoustic analogy is used to predict acoustic propaga-  
 21 tion to the farfield from the near-field time-resolved flow data obtained from CFD. The FW-H  
 22 formulation can be expressed in the following differential form.

$$\left( \frac{\partial^2}{\partial t^2} - c_o^2 \frac{\partial^2}{\partial x_i \partial x_i} \right) (H(f) \rho') = \frac{\partial^2}{\partial x_i \partial x_j} (T_{ij} H(f)) - \frac{\partial}{\partial x_i} (F_i \delta(f)) + \frac{\partial}{\partial t} (Q \delta(f)) \quad (6)$$

1 where,

$$\begin{aligned} T_{ij} &= \rho u_i u_j + P_{ij} - c_o^2 \rho' \delta_{ij}, \\ F_i &= (P_{ij} + \rho u_i (u_j - v_j)) \partial f / \partial x_j, \text{ and} \\ Q &= (\rho_o v_i + \rho (u_i - v_i)) \partial f / \partial x_j. \end{aligned} \tag{7}$$

2  $P_{ij}$  is the compressive stress tensor,  $f$  is the function that describes the integration surface, and  $H(f)$   
3 is the Heaviside function. Integration of Eq. (6) results in an unsteady mass addition (monopole)  
4 term corresponding to  $Q$ , an unsteady force (dipole) term corresponding to  $F_i$ , and an unsteady  
5 volume (quadrupole) term corresponding to  $T_{ij}$ . The flow speed is small in the simulations presented  
6 here, and the volume integral term corresponding to  $T_{ij}$  can be ignored. Therefore, only the surface  
7 integrals are required to be computed. The surface used for acoustic prediction using such an  
8 acoustic analogy is often called a Kirchoff surface. A “porous” Kirchoff surface enclosing the  
9 acoustic sources is used here that allows flow to pass through. Figure 5 shows the Kirchoff surface  
used in the current predictions.

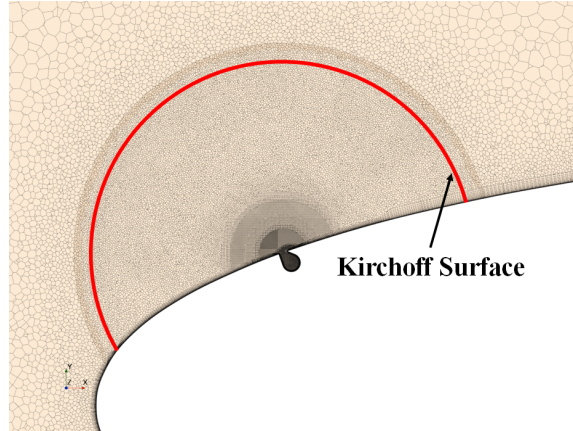


Figure 5: The integration (Kirchoff) surface used in the present work to predict farfield acoustics using the FW-H acoustic analogy.

10

11 *Atmospheric absorption.* Atmospheric absorption effects on sound propagation must be accounted  
12 for in the numerical predictions to compare with experimental measurements. The atmospheric  
13 absorption coefficients are calculated using the ANSI standard (Bass et al., 1995; ISO 9613-1:1996)

1 for the tonal frequencies in the predicted spectra with the temperature, relative humidity, and  
 2 pressure set as 293 K, 50% and 1 atm, respectively.

### 3 4. Experimental measurements

4 The baseline blade uses the NACA 0012 profile that is extruded along the span. The two  
 5 deterrent configurations, HF and LF (see Table 1), and the baseline blade were tested in the  
 6 Virginia Tech Stability Wind Tunnel to characterize the acoustic performance of the deterrents for  
 7 varying freestream flow velocity ( $V_\infty$ ) and blade angle of attack ( $\alpha$ ). The full test matrix is provided  
 8 in Table 2.

Table 2: Test matrix to evaluate the passive ultrasonic deterrents. The baseline blade (Base) is the NACA 0012 model without any deterrent installed; the HF and LF are the deterrent configurations from Table 1. The chord-based Reynolds number ( $Re_c$ ) varies with the freestream flow speed ( $V_\infty$ ).

$V_\infty$ [m/s]	$\alpha$ [deg]	<i>Configuration</i>	$Re_c$ ( $\times 10^6$ )
30	0	Base, LF	1.67
35	0	Base, LF	1.94
40	0	Base, LF	2.22
45	0	Base, LF	2.50
50	0	Base, LF	2.75
55	0	Base, HF, LF	3.02
60	0, 2, 4	Base, HF, LF	3.27

9 Figure 6 plots the spectrogram of acoustic radiation from the HF deterrent at  $V_\infty = 60$  m/s and  
 10  $\alpha = 0^\circ$ . The signal is acoustic pressure measured at the center of the microphone array. Steady  
 11 tones are observed at  $\sim 24$  and 48 kHz. No deterministic modulation in frequency or amplitude is  
 12 observed.

#### 13 4.1. Variation with flow speed

14 Figure 7 plots the filtered sound pressure spectra at different flow speeds ( $V_\infty$ ) for the HF and LF  
 15 deterrents. The spectra are shown only for selected values of  $V_\infty$ . The deterrents do not produce  
 16 sound below a critical flow speed, which is deterrent-specific. This critical (minimum) speed is

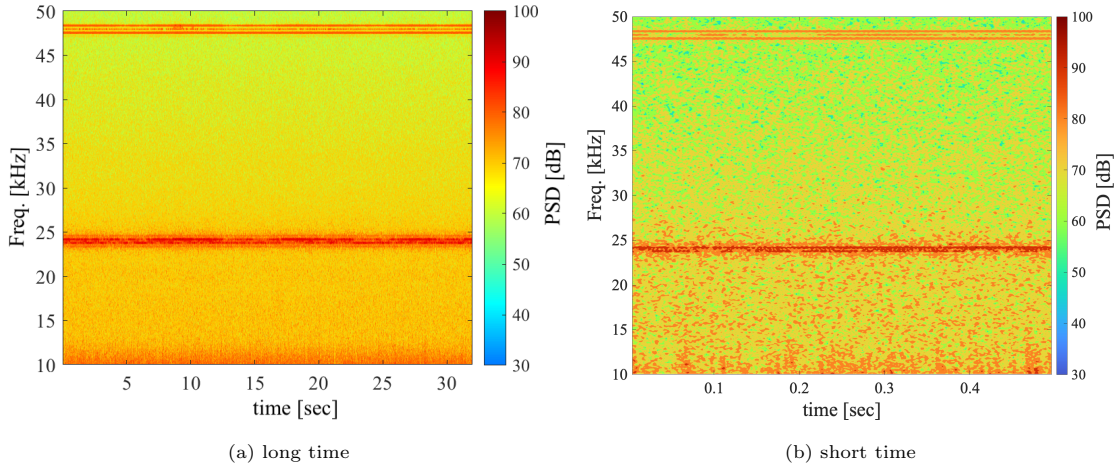


Figure 6: Spectrograms of acoustic pressure for the HF deterrent measured by the center microphone of the phased array over a long time (a) and over a short time (b). Steady acoustic radiation is observed. Operating conditions:  $V_\infty = 60$  m/s and  $\alpha = 0^\circ$

1 called the ‘onset’ speed. The onset flow speed is a function of the geometry (size) of the resonator,  
 2 with the larger resonator having a smaller  $V_{\infty, \min}$ . These observations are consistent with prior  
 3 experiments (Gharib and Roshko, 1987; Krishnamurty, 1955; Sarohia, 1975). The onset speeds for  
 4 the HF and LF deterrents are between 55 – 60 m/s and 30 – 35 m/s, respectively (see Fig. 7).

5 Beyond the onset speed, the HF deterrent generates a high-amplitude tone at the fundamental  
 6 frequency of 23.8 kHz and the second harmonic at 47.6 kHz. Higher harmonics likely exist, but the  
 7 microphones do not capture sound above 60 kHz. The noise radiation from the baseline blade (no  
 8 deterrent) at  $V_\infty = 60$  m/s is shown in gray in Fig. 7a. Other than the tones at the fundamental  
 9 and the second harmonic of the HF resonators, the radiated acoustic spectrum with the deterrent  
 10 installed follows that of the baseline blade, suggesting that the sleeve used to mount the deterrents  
 11 does not introduce significant additional noise.

12 No radiation is observed at  $V_\infty = 30$  m/s (which is below the onset speed) for the LF deterrent.  
 13 At  $V_\infty = 35$  m/s, the fundamental tone for the LF deterrent ( $\sim 10.8$  kHz) and several higher  
 14 harmonics are observed. There is also discernible acoustic radiation at this  $V_\infty$  in a sub-harmonic  
 15 of the fundamental, at around 5.6 kHz. As  $V_\infty$  increases to 60 m/s, the sub-harmonic tone subsides,  
 16 and the spectrum shows prominent tones at the fundamental and higher harmonics.

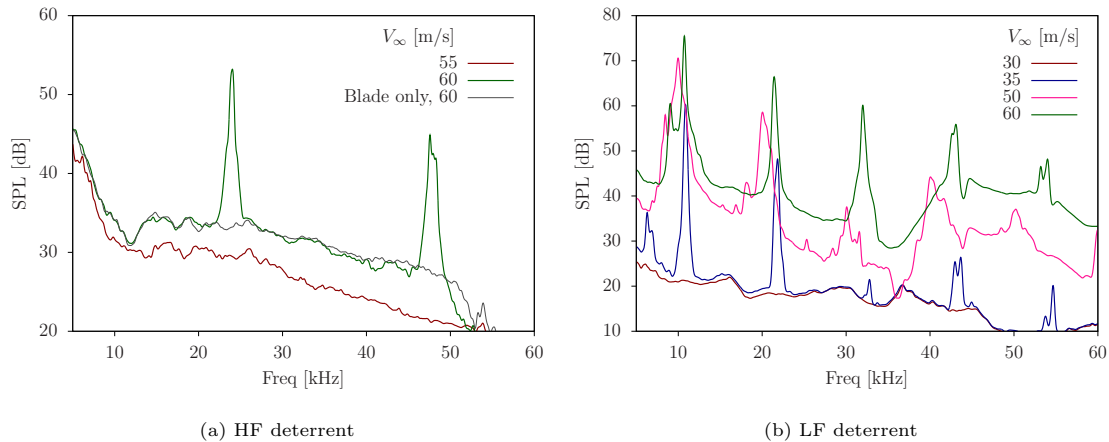


Figure 7: Variation with flow speed ( $V_\infty$ ) of the filtered SPL spectra for the (a) HF deterrent and the (b) LF deterrent. The gray line in panel (a) is the filtered spectrum of the acoustic radiation from the baseline blade without any deterrent installed. Filtering broadens the spectral peaks and makes the tonal SPL values look lower than they are.

#### 1 4.2. Variation with angle of attack

2 The angle of attack is varied by pitching the blade about the quarter-chord line. Figure 8 plots  
 3 the SPL spectra of the HF and LF deterrents for three angles of attack,  $\alpha = 0^\circ$ ,  $2^\circ$ , and  $4^\circ$ . It  
 4 should be noted that  $\alpha$  is defined for the blade; the resonators are engraved on both sides of the  
 5 sleeve that wraps around the leading edge of the blade. Hence, one set of resonators is on the suction  
 6 side while the other is on the pressure side of the blade. The acoustic array is on the Starboard side  
 7 of the tunnel. As  $\alpha$  increases, the blade leading edge is tilted towards the microphone array. Blade  
 8 pitching, therefore, affects not only the aerodynamics but also the distance and the angle between  
 9 the acoustic source (deterrent) and the microphone array. On average, the increase in  $\alpha$  from  $0^\circ$   
 10 to  $4^\circ$  increases the radiated acoustic intensity. This is due to the increase in local flow speed due  
 11 to the acceleration of the flow around the airfoil leading edge on the suction side of the blade with  
 12 increasing  $\alpha$ . There is also a small increase ( $< 0.3$  kHz) in the peak frequency for the HF deterrent  
 13 with increasing  $\alpha$ . This is consistent with the numerical results presented in Section 5.2; see Fig. 16,  
 14 which shows an increase in the fundamental resonance frequency with flow speed.

15 For the LF deterrent, increasing  $\alpha$  leads to the generation of non-harmonic tones. Even after  
 16 filtering, several peaks are observed around the broad spectral peaks at harmonics of the resonance  
 17 frequency (see Fig. 8b). While the trend of increasing acoustic intensity with  $\alpha$  is apparent, the



1 frequency shift is difficult to ascertain for the LF deterrent due to the several additional peaks  
 2 that vary with the size of the Gaussian filter used. The measurements show that both deterrents  
 generate tones at the desired frequencies for the three  $\alpha$  values considered.

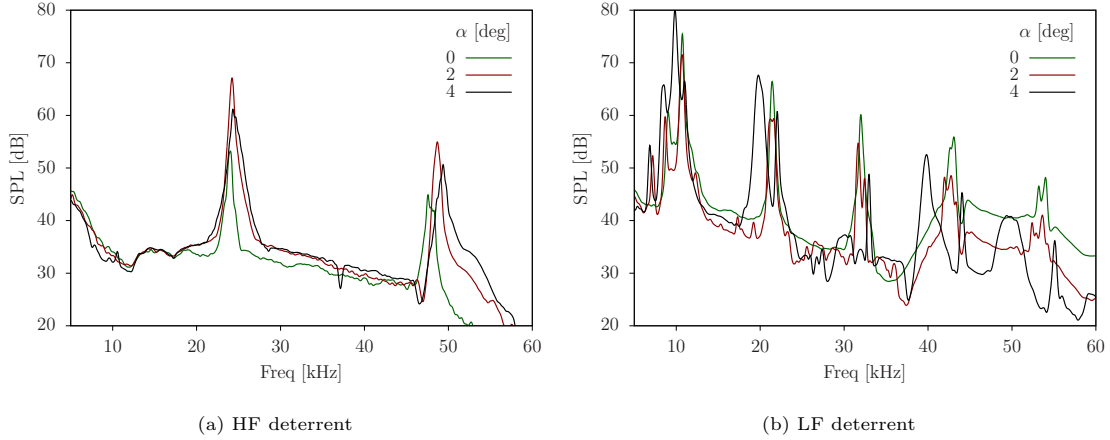


Figure 8: Variation with blade angle of attack ( $\alpha$ ) of the filtered SPL spectra for the (a) HF deterrent and the (b) LF deterrent, at  $V_\infty = 60$  m/s.

3

#### 4 4.3. Beamform maps

5 Beamform maps provide a visual illustration of the physical location of acoustic sources. The  
 6 beamform maps are computed using 1/12th octave band spectra to reduce uncertainty. Figure 9  
 7 shows the beamform maps for the LF deterrent at  $V_\infty = 60$  m/s and  $\alpha = 0^\circ$ . Two maps are shown  
 8 with center frequencies 10.6 kHz and 11.2 kHz; the fundamental frequency of the resonators in the  
 9 LF deterrent is  $\sim 10.8$  kHz. At 10.6 kHz, the map shows three point sources, one near the center  
 10 and two at the span ends of the deterrent (Fig. 9a). At 11.2 kHz frequency, the map shows a  
 11 strong source across the span of the deterrent. The deterrent is much louder (at least 10 dB) than  
 12 the noise produced by the airfoil and the tunnel at these frequencies. Therefore, the only acoustic  
 13 sources in the maps are at the deterrent location. Similar results were observed at higher  $\alpha$  for the  
 14 LF deterrent.

15 The beamform maps for the HF deterrent (Fig. 10) do not show a clear source location, which was  
 16 unexpected because the integrated spectra (see Figs. 7a and 8a) show clear tones at the harmonics of  
 17 the resonance frequency. Appendix B explains why the acoustic source locations are not accurately  
 18 identified in the beamform maps, particularly for the HF deterrent.

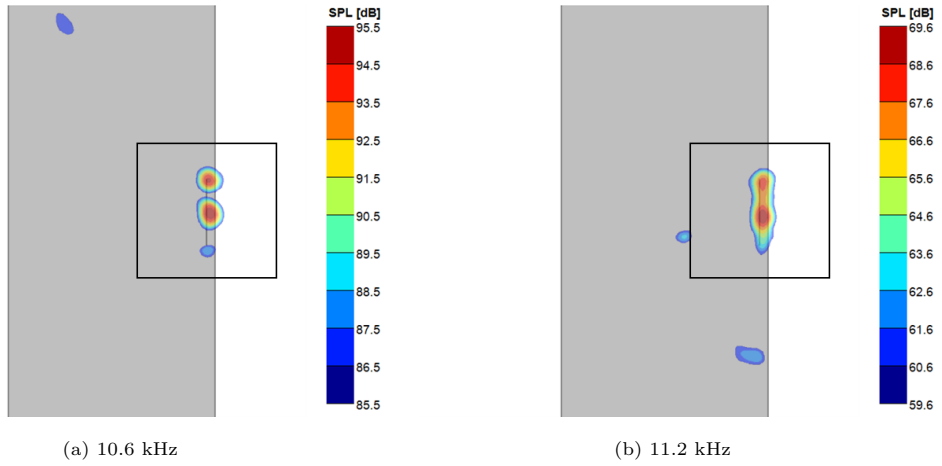


Figure 9: Beamform maps at two frequencies around the fundamental frequency of the LF deterrent superimposed on the planform of the airfoil (gray box). The black rectangle shows the integration region used to obtain the acoustic spectra.  $V_\infty = 60$  m/s and  $\alpha = 0^\circ$ .

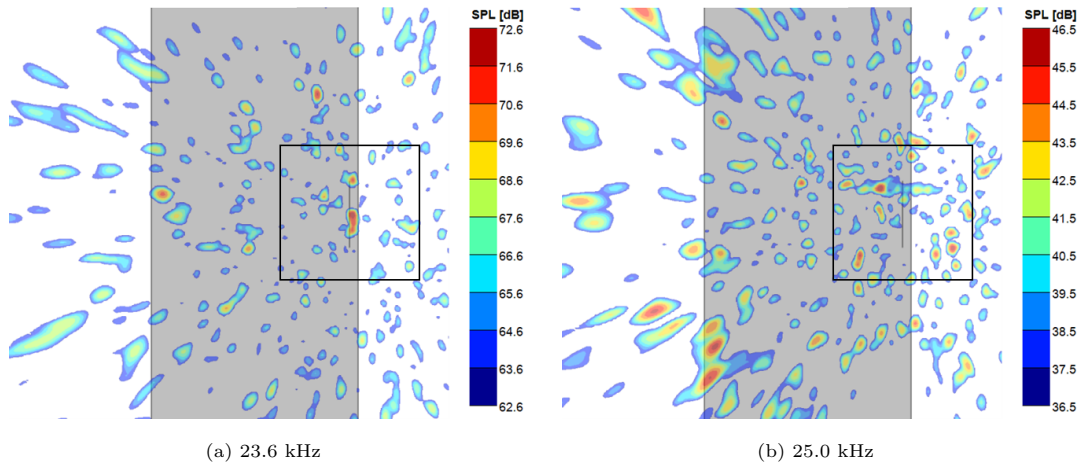


Figure 10: Beamform maps around the fundamental frequency of the HF deterrent superimposed on the planform of the airfoil (gray box). The black rectangle shows the integration region used to obtain the acoustic spectra.  $V_\infty = 60$  m/s and  $\alpha = 0^\circ$ .

## 1 5. Computational results

2 Numerical simulations are performed to supplement the measurements. The baseline blade and  
 3 the HF deterrent are simulated. Two-dimensional (2-D) simulations are performed first to assess the  
 4 impact of the deterrent on the aerodynamic performance of the blade/airfoil. The 2-D simulations

1 are also used to evaluate the acoustic performance of the passive whistle; their results are compared  
2 qualitatively with measurements. While acoustic radiation is a 3-D phenomenon, (ultra)sound  
3 generation in the passive whistles is primarily two-dimensional; 3-D effects on acoustic sources  
4 are investigated in Section 5.3. Appendix C summarizes the results of a mesh sensitivity study  
5 to identify the optimum mesh spacing and time step for the simulations; the baseline mesh (see  
6 Appendix C) and  $\Delta t = 2.5E - 07$  are used for the simulations.

7 Two-dimensional simulations are performed over a range of freestream flow speeds ( $V_\infty$ ), corre-  
8 sponding to the blade speed in the outer 50% of a typical utility-scale wind turbine rotor. Variation  
9 with airfoil angle of attack ( $\alpha$ ) is also evaluated. Three-dimensional CAA simulations are then  
10 performed to (a) quantitatively compare against acoustic measurements made in the Virginia Tech  
11 Stability Wind Tunnel, (b) investigate the three-dimensional aerodynamic and acoustic interactions  
12 between adjacent resonators in the passive deterrents, and (c) assess the directivity of the radiated  
13 ultrasound.

14 We first present the 2-D results. Figure 11a shows the computational domain, the mesh, and the  
15 boundary conditions used for the simulations. Figure 11b shows a zoomed view of the mesh inside  
16 and around the resonating cavity. The resonator is only placed on the suction side of the airfoil  
17 (at 4% chord) to reduce the mesh size and the computational cost. Freestream Mach number, flow  
18 direction, and stagnation pressure and temperature are specified at the inlet boundaries. Static  
19 pressure at the outlet boundary is set to atmospheric pressure. The airfoil surface is treated as a  
20 no-slip, adiabatic wall.

### 21 5.1. Aerodynamic performance

22 The aerodynamic influence of the deterrent on the blade is evaluated by comparing the airfoil  
23 polars between the baseline and the deterrent configurations. The baseline is the NACA 0012 airfoil,  
24 and the HF resonator is used for the deterrent.

25 Figure 12 compares the lift and drag coefficients ( $c_l$  and  $c_d$  respectively) and the lift-to-drag ratio  
26 ( $c_l/c_d$ ) between the baseline blade and the deterrent configurations. Also plotted are XFOIL (Drela,  
27 1989) predictions for reference. At small  $\alpha$ , the CFD predictions are in good agreement with XFOIL  
28 and there is negligible impact on the aerodynamic performance of the blade because of the deterrent.  
29 For larger  $\alpha$  ( $> 8^\circ$ ), CFD predicts a higher drag value for the baseline blade than XFOIL. At these  
30 high  $\alpha$  values, the boundary layer is thick near the airfoil's trailing edge and may also be partially

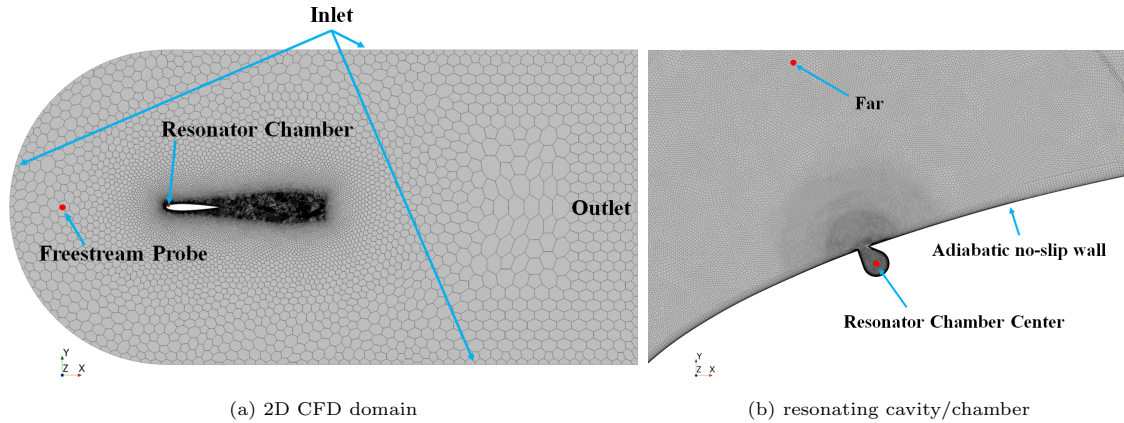


Figure 11: The computational mesh used for the 2D simulations. (a) the full computational domain, and (b) a zoomed view of the mesh inside and around the resonating cavity.

1 separated. Since the objective of this study is ultrasound generation by the passive deterrents,  
 2 which are mounted near the airfoil leading edge, the mesh is coarsened towards the airfoil trailing  
 3 edge to save computational time. This could be a reason for the overprediction of drag ( $c_d$ ) and  
 4 the underprediction of  $c_l/c_d$  in CFD. The accuracy of XFOIL is also questionable at high  $\alpha$  when  
 5 separated flow can occur near the trailing edge. Nevertheless, the CFD predictions show little  
 6 impact of the deterrent on the aerodynamic performance of the airfoil/blade over the range of  $\alpha$   
 tested.

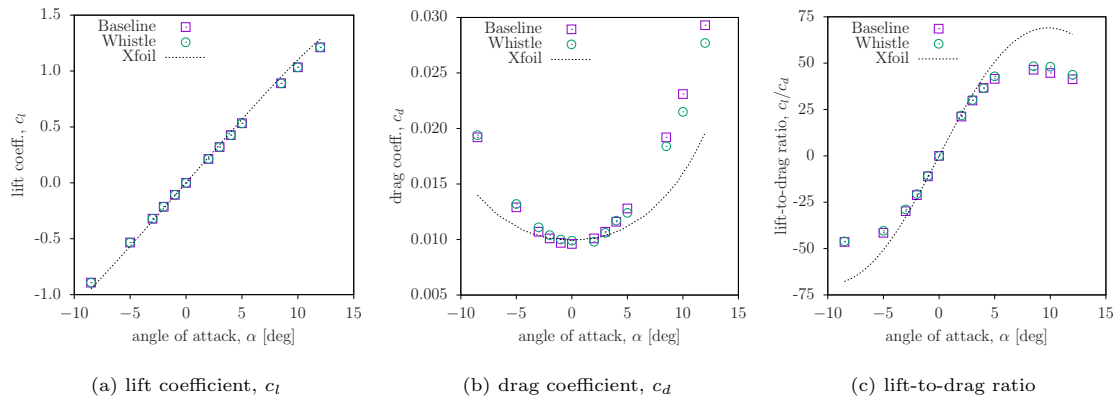


Figure 12: CFD predictions of the lift and drag coefficients and lift-to-drag ratio. XFOIL predictions are shown for reference.

1 Figure 13 plots the distributions of coefficients of pressure and skin friction ( $c_p$  and  $c_f$  respec-  
 2 tively) on the airfoil surface at  $\alpha = 8.5^\circ$ , where  $c_l/c_d$  is maximum. Wind turbine rotor blades  
 3 operate at  $\alpha$  corresponding to  $\max(c_l/c_d)$  at the design point. CFD and XFOIL results are in  
 4 good agreement. Moreover, the difference between the results for the baseline blade and the blade  
 5 with a deterrent installed is negligible. We can, therefore, conclude that these deterrents will not  
 6 adversely impact the aerodynamic performance of wind turbines if they are engraved into the rotor  
 7 blades; the aerodynamic impact of the sleeve mounting approach (used in the current laboratory  
 experiments) is not assessed.

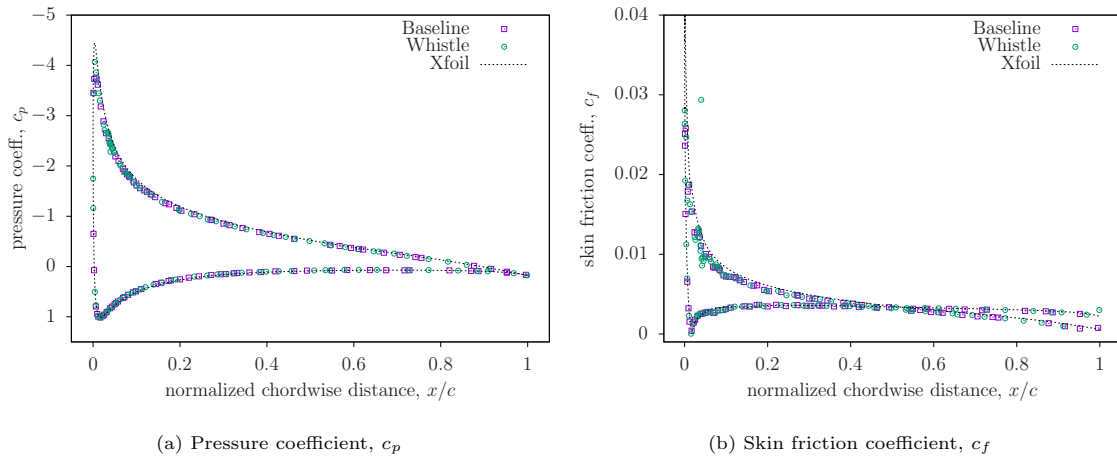


Figure 13: CFD predicted distributions of pressure and skin friction coefficients on the airfoil surface at angle-of-attack,  $\alpha = 8.5^\circ$ . Also plotted for reference are XFOIL predictions.

8

## 9 5.2. Acoustic performance

10 Time-resolved, 2-D simulations are performed for the HF deterrent. Figure 14 shows a visual-  
 11 ization of the radiating acoustic field via instantaneous pressure contours. Strong tonal radiation  
 12 originating from the resonator is observed in the figure.

13 Time-accurate pressure data is collected at two locations in the computational domain. One  
 14 probe (Probe A) is located in the center of the resonating chamber, and another (Probe B) is located  
 15 10 mm away from the chamber opening. Fourier analysis of the pressure time history at Probe  
 16 B is performed to generate the power spectral density (PSD) of the signal. Figure 15b presents a  
 17 qualitative comparison of the pressure PSD spectra between the 2-D predictions and measurements.

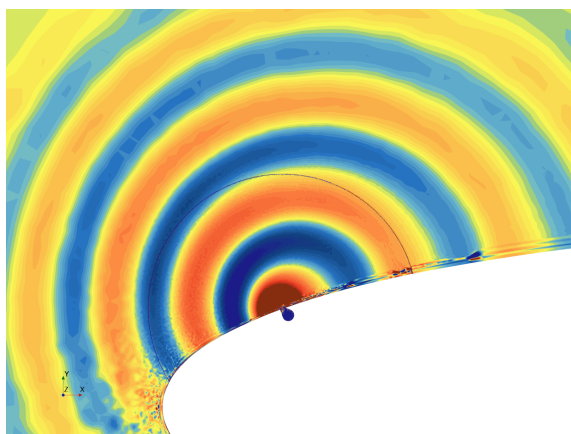
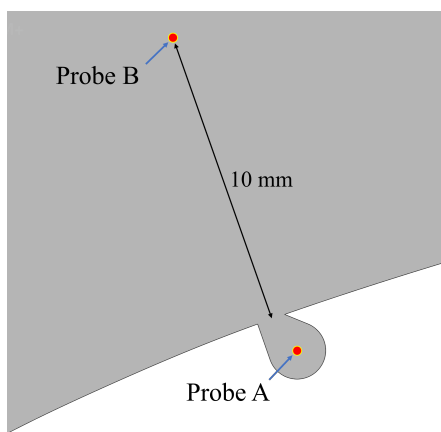
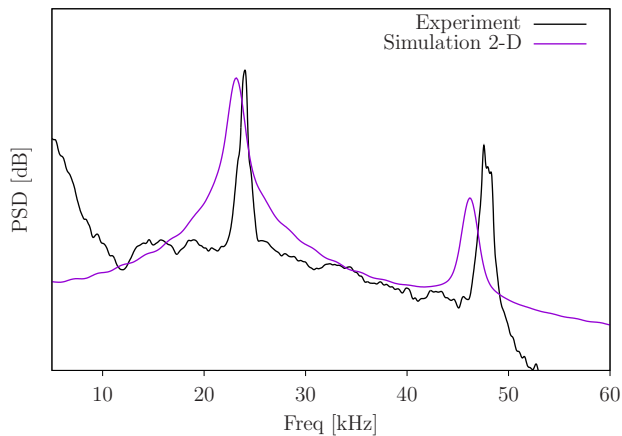


Figure 14: Radiated acoustic field visualized with instantaneous pressure contours in a 2-D simulation of the HF deterrent.

- 1 The ordinate values are not shown in the figure as they are irrelevant; the measurements are made
- 2 in the acoustic farfield where the acoustic waves radiate in a 3-D space, whereas the numerical
- 3 result is a 2-D prediction (radiation restricted to a 2-D space) at a point close to the airfoil. The
- 4 numerical prediction captures the measured frequencies of the fundamental tone and the second harmonic.



(a) Probe locations



(b) PSD spectra

Figure 15: Sample 2-D CFD simulation: (a) locations where time accurate data is sampled, and (b) a qualitative comparison of the radiated acoustic spectra between 2-D CFD (Probe B) and experiments ( $V_\infty = 60$  m/s,  $\alpha = 0^\circ$ ).

1 5.2.1. Variation with flow speed

2 Two-dimensional simulations are conducted for  $V_\infty$  values ranging from 21 m/s to 96 m/s for  
 3 both HF and LF deterrents. A Fourier analysis of the unsteady pressure signal at Probe A (located  
 4 at the center of the resonating chamber) is performed to identify the peak radiation frequency.  
 5 Figure 16 illustrates the variation of peak frequencies with  $V_\infty$  for the two deterrents. The figure  
 6 also presents experimental data and theoretical estimates for the Helmholtz resonance frequency  
 and the first Rossiter mode frequency.

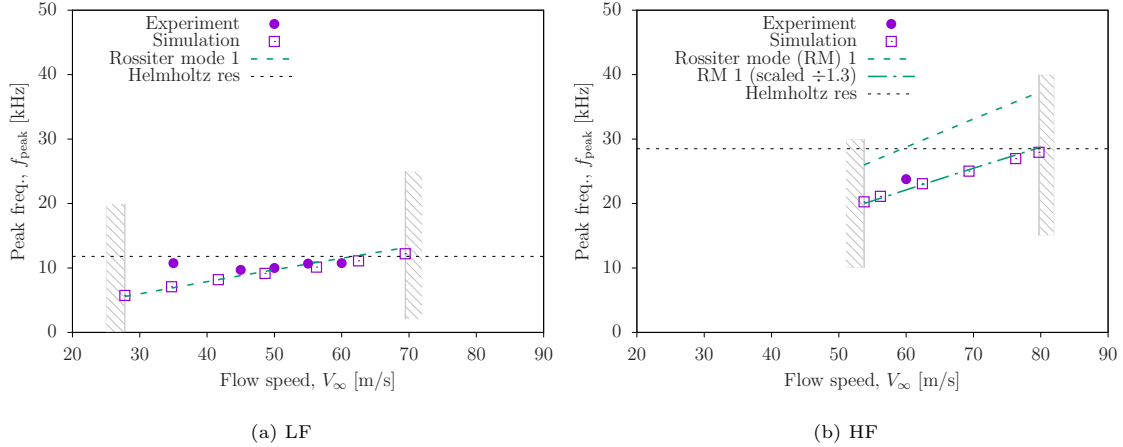


Figure 16: Variation of the peak (fundamental) frequency with  $V_\infty$  for the LF (a) and HF (b) deterrents. The gray hashed regions indicates the lower and upper limits on  $V_\infty$  beyond which acoustic radiation does not occur. The solid lines show the 2-D CFD simulation predictions while the hollow circles show the measured data. The dotted horizontal line shows the estimated (theoretical) Helmholtz resonance frequency, and the green dashed line shows the first Rossiter mode frequency for the deterrent based on freestream velocity. The label ‘RM 1 (scaled)’ refers to the Rossiter mode frequency scaled by 1.3 to compare the trend.

7  
 8 Resonance occurs when the freestream flow speed,  $V_\infty$ , exceeds the onset speed ( $V_{\infty, \text{min}}$ ). The  
 9 onset of oscillations/resonance is observed in both simulations and experiments (Figs. 7 and 16).  
 10 We also identify an upper limit on  $V_\infty$  beyond which oscillations do not occur in our simulations  
 11 (Figs. 16a and 16b). This phenomenon was observed by Mongeau et al. (1997) in their measurements  
 12 of pressure oscillations in scaled models of passenger cars. While the theoretical model of Covert  
 13 (1970) does not predict this upper limit due to their inviscid flow assumption, they state that  
 14 there is experimental evidence for oscillations ceasing as velocity exceeds a critical maximum value.  
 15  $V_{\infty, \text{max}}$  was not reached in our experiments due to the tunnel’s maximum safe operating speed limit

1 of 60 m/s.

2 In the  $V_\infty$  range where acoustic radiation occurs, the fundamental frequency is predicted to  
3 increase almost linearly with  $V_\infty$ , closely matching the theoretical estimate for the first Rossiter  
4 mode frequency. The rate of increase is greater for the HF deterrent compared to the LF deterrent.  
5 While the Helmholtz resonance frequency remains constant, the frequency of the Rossiter mode  
6 varies linearly with flow speed above the cavity. In the case of spatially varying mean flow, it is  
7 uncertain at which point the flow speed should be evaluated. Here, the freestream flow speed,  $V_\infty$ ,  
8 is used, which works well for the LF deterrent but needs to be scaled down by a factor of 1.3 for  
9 the HF deterrent to align with the CFD simulations. The measured data for the LF deterrent  
10 follows the linear trend predicted by CFD (Fig. 16a), except at  $V_\infty = 35$  m/s. There are competing  
11 resonance mechanisms - Helmholtz and Rossiter modes. At this flow speed, the system appears to  
12 lock into Helmholtz resonance in the experiments, while simulations indicate that the Rossiter mode  
13 mechanism dominates. For the HF deterrent, measurements are only available at  $V_\infty = 60$  m/s, and  
14 this data point aligns with the CFD-predicted trend line, consistent with the theoretical estimate  
15 of the first Rossiter mode frequency (Fig. 16b).

### 16 5.2.2. Variation with angle-of-attack

17 The acoustic performance of the HF deterrent is numerically investigated for  $\alpha$  values ranging  
18 from  $-8.5^\circ$  to  $12^\circ$ , with experimental data available at  $\alpha = 0^\circ, 2^\circ, 4^\circ$ . Similar to  $V_{\infty, \min}$ , there  
19 is a minimum  $\alpha$  ( $\alpha_{\min} = -1^\circ$ ) below which acoustic radiation does not occur. The fundamental  
20 frequency at  $\alpha_{\min}$  is 20.3 kHz, the same frequency observed at  $V_{\infty, \min}$  (Fig. 16). For  $\alpha < \alpha_{\min}$ , the  
21 local flow speed at the deterrent location is below the onset speed. Therefore, the limits on  $\alpha$  stem  
22 from the constraints on flow speed that determine whether resonance is excited. The maximum  $\alpha$   
23 for which radiation is observed in the simulations is  $\alpha_{\max} = 12^\circ$ . Note that this only applies to  
24 simulations where the resonator is modeled solely on the suction side of the airfoil.

25 Figure 17 shows that the predicted peak frequency increases with  $\alpha$ . This may be due to the  
26 increase in local flow velocity with  $\alpha$  in the linear  $C_l - \alpha$  range (small  $\alpha$ ). The variation of the  
27 first Rossiter mode frequency is also plotted, showing a linear increase with  $\alpha$ ; scaling it by 1.5  
28 still indicates a much larger increase with  $\alpha$  than in the simulations. Since the freestream velocity,  
29  $V_\infty$  does not change with  $\alpha$ , we use the edge velocity (derived from inviscid XFOIL calculations)  
30 to compute the Rossiter mode frequency. The discrepancy between the variations of the Rossiter



1 mode frequency and the CFD predictions suggests that the inviscid edge velocity may not be the  
 2 appropriate velocity scale, and that the velocity at a point in the boundary layer might be more  
 3 suitable. The measured data roughly aligns with the CFD predicted trend; however, the variation  
 with  $\alpha$  is even smaller in the experiments.

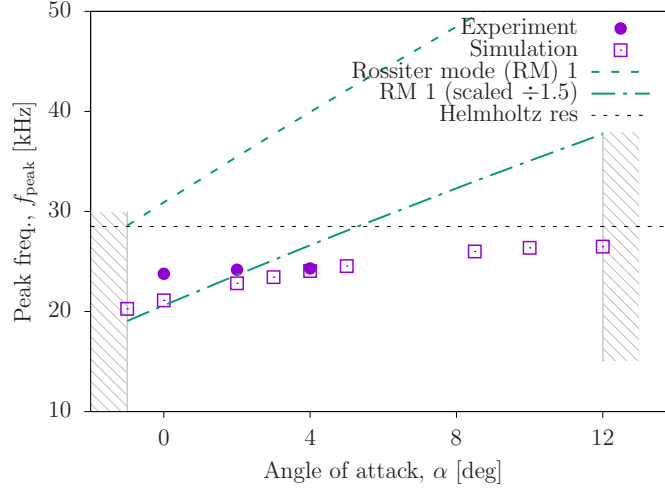


Figure 17: Peak frequency ( $f_{\text{peak}}$ ) variation with angle-of-attack ( $\alpha$ ); theoretical estimate of the Helmholtz resonance frequency,  $f_R$  is shown as the horizontal dashed line. The hashed regions bound the range of  $\alpha$  over which acoustic radiation is predicted.

4  
 5 The resonators were engraved on both sides of the sleeve (blade) in the experimental model. An  
 6 increase in  $\alpha$  results in an increase in the local flow velocity for the resonators on the suction side  
 7 of the blade but a reduction for the resonators on the pressure side. A consequence of this would  
 8 be an increase in the resonance frequency of the resonators on the suction side and a reduction for  
 9 the resonators on the pressure side, resulting in two peaks relatively close (in frequency) to each  
 10 other. This can be observed for the LF deterrent in Fig. 8b, where the frequency separation is  
 11 larger than the filter width. The two-peak pattern is unclear for the HF deterrent (Fig. 8a) because  
 12 the pressure-side resonators fall below  $\alpha_{\text{min}}$  and are unable to establish resonance.

### 13 5.3. Three-dimensional analysis

14 While the two-dimensional simulations provide valuable qualitative insights and design guidance,  
 15 they cannot be quantitatively compared with experimental data. Therefore, three-dimensional (3-  
 16 D) simulations are conducted to validate the predictions. The 3-D mesh is generated by extruding

1 the 2-D mesh along the span. Each deterrent is simulated in two configurations: in the first config-  
 2 uration, one resonator is modeled, while in the second configuration, two resonators are modeled.  
 3 The computational domain spans from  $z = -3$  mm to  $+3$  mm for the one-resonator configuration  
 4 and from  $z = -6$  mm to  $+6$  mm for the two-resonator configuration. Periodic boundary conditions  
 5 are applied in the  $z$  direction for both models; the boundary conditions on the other surfaces are  
 6 consistent with those used in the 2-D simulations. Figure 18 shows an isometric view of the two-  
 7 resonator numerical model. As in the 2-D simulations, the deterrent is modeled only on the suction  
 side of the airfoil.

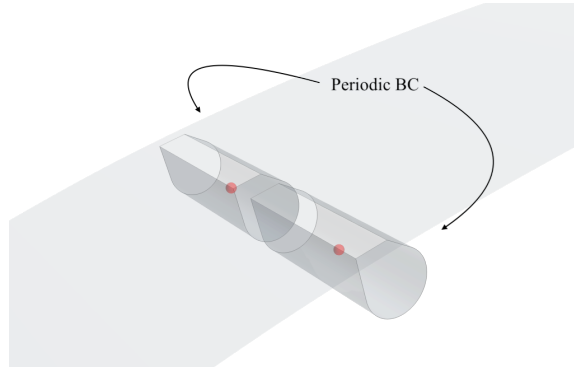


Figure 18: An isometric view of the two-resonator computational model. Periodic boundary conditions are used in the span direction. The red points are data probes placed at the center of each resonator in the numerical model. Time-accurate pressure data is collected at these probe locations.

8

9 Given the focus on ultrasound radiation, only the results for the HF deterrent at  $V_\infty = 60$  m/s  
 10 are discussed. Figure 19a compares the PSD spectra of the predicted pressure signal at the center of  
 11 the resonator (Probe A) for the one-resonator (1R), two-resonator (2R), and 2-D simulations. The  
 12 spectrum from the 2-D simulation is similar to the 3-D prediction for the 1R model. In contrast,  
 13 the 3-D simulation result for the 2R model exhibits higher signal power for both broadband and  
 14 tonal sounds, with a higher peak frequency (fundamental) as well.

15 Analysis of the pressure time signal (Fig. 19b) for the 2R model reveals that the pressures at  
 16 the centers of the two resonators are nearly out of phase. This out-of-phase relationship between  
 17 resonators was also observed in our previous work on aerodynamic ultrasonic whistles powered  
 18 by compressed air (Zeng and Sharma, 2023, 2025). The out-of-phase oscillation between adjacent  
 19 resonators enhances their response, leading to greater amplification of unsteadiness; as a result,

1 the PSD spectrum for the 2R configuration is approximately 20 dB greater than that of the 1R  
 2 configuration. It is important to note that these spectra represent the hydrodynamic pressure  
 measured at the center of a resonator, not the radiating acoustic pressure.

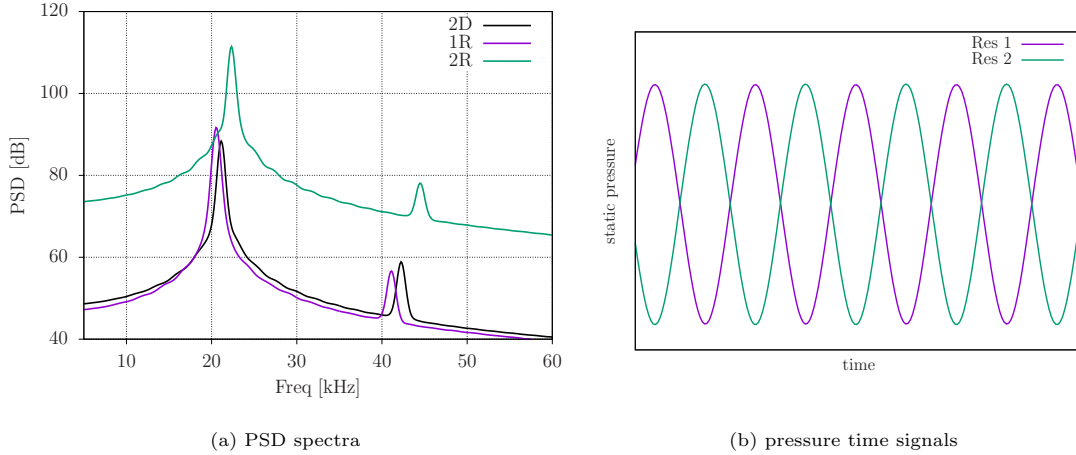


Figure 19: PSD spectra at the resonator chamber center compared between different simulations (a), and time history of pressure measured at the centers of the two resonators in the two-resonator simulation.

3

4 Far-field ultrasound radiation is computed by solving the FW-H equation. The FW-H integra-  
 5 tion (Kirchoff) surface is illustrated in Fig. 5; it extends through the entire computational domain  
 6 in the span direction. Since the deterrent span in the simulation is smaller than in the experiments,  
 7 corrections have to be applied to the predicted noise radiation in order to compare with the mea-  
 8 surements; Appendix D explains how these corrections are obtained and the approximations that  
 9 are involved. Figure 20 shows the locations of the observers where the radiated acoustic field is  
 10 predicted. These observer locations are arranged in a line (array) parallel to the blade leading edge  
 11 (along  $z$ ) and range from  $z = -144$  mm to  $+144$  mm. This range corresponds to the span over  
 12 which the resonators are positioned on the deterrents (HF and LF) tested in the wind tunnel.

13 The center of the observer array is located at a  $90^\circ$  polar angle (measured from upstream)  
 14 and is 1 m directly above the suction side of the blade leading edge, aligning with the center of  
 15 the microphone array used in the experiments. For the 1R model, the distance between adjacent  
 16 observers is 6 mm, which matches the span of the numerical model. The 2R model has double  
 17 the span, so the observers are spaced 12 mm apart. By summing (with appropriate phases) the  
 18 predicted sound signals at all observer locations along each array, we obtain the signal that would

1 be measured at the center observer location for the full-size deterrent (with a 288 mm span) (see  
 Appendix D).

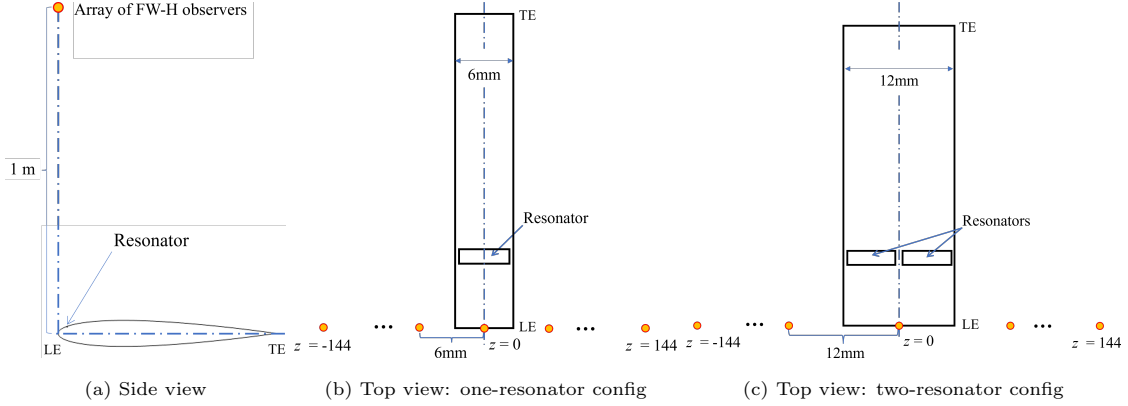


Figure 20: Observer locations: (a) side view showing that the observer array is located at  $90^\circ$  polar angle, (b & c) top views of the one-resonator and two-resonator models; the array of observers spans  $z = -144$  mm to  $+144$  mm, and the spacing between adjacent operators is equal to the span of the blade simulated ( $= 6$  mm and  $12$  mm for one- and two-resonator models respectively)

2

3 We first examine the farfield pressure PSD spectra predictions without span correction. The  
 4 simulated spans are 6 mm for the 1R configuration and 12 mm for the 2R configuration. Farfield  
 5 acoustics is compared at the observer located 1 m away at a  $90^\circ$  polar angle (see Figs. 20a and 21a).  
 6 The result for the one-resonator model appears as expected, with the fundamental resonance fre-  
 7 quency peak exhibiting higher intensity than the second harmonic. In contrast, the second harmonic  
 8 for the 2R model is stronger than the fundamental, despite the hydrodynamic pressure inside the  
 9 resonator showing greater intensity at the fundamental frequency (Fig. 19a). This discrepancy arises  
 10 because the unsteady pressures in the two resonators in the 2R model are out of phase (Fig. 19b),  
 11 resulting in partial cancellation of the radiated sound for the odd harmonics of the fundamental  
 12 frequency.

13 The 2R simulation clearly demonstrates a strong correlation between adjacent resonators. How-  
 14 ever, the degree of correlation between the 48 resonators across the entire span of the physical  
 15 deterrent is unknown. To address this, we make two assumptions for our far-field predictions: (1)  
 16 all resonators in the deterrent are completely correlated, and (2) the resonators are completely  
 17 uncorrelated. We anticipate that these two assumptions will bound the actual far-field acoustic  
 18 intensity.

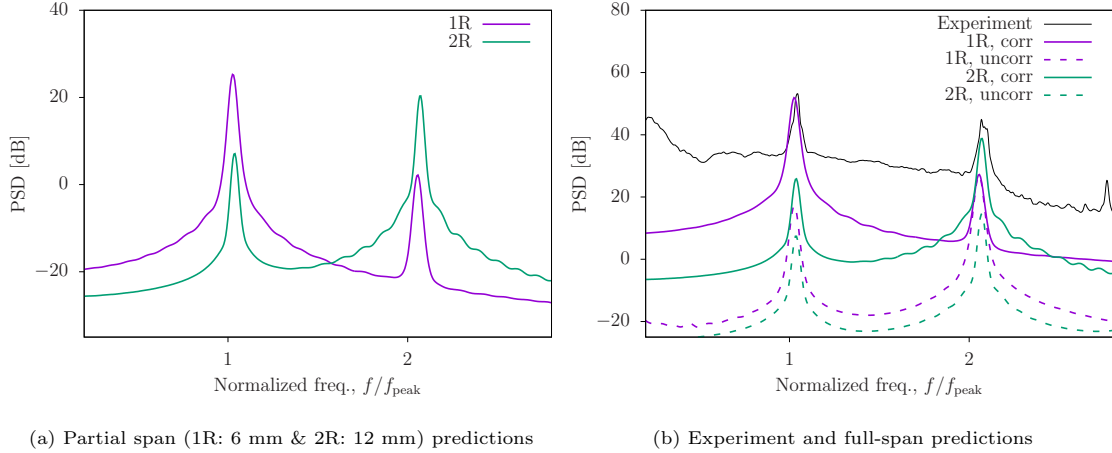


Figure 21: Predicted PSD spectra for the HF deterrent at the observer located 1 m directly above the airfoil leading edge ( $90^\circ$  polar angle). (a) Predictions from the 6 mm-span one-resonator configuration (1R) and 12 mm-span for the two-resonator configuration (2R), and (b) experimental data and predictions for the full-span (288 mm) HF deterrent for the two configurations. For the full-span predictions, the signals from the different resonators are assumed to be fully correlated (solid lines) and completely uncorrelated (dashed lines).

Figure 21b compares the predicted spectra from the full-span (288 mm) deterrent at the observer 1 m away at a  $90^\circ$  polar angle. The broadband noise cannot be directly compared, as the major source of this noise is airfoil self-noise, which is not included in the simulations. At first glance, it seems that the peak PSD at the fundamental frequency is well predicted by the 1R model when assuming complete correlation. However, it is important to note that the frequency bandwidths of the spectral peaks differ between the experiments and predictions. A more relevant metric for tonal sound is the tonal sound pressure level (SPL), obtained by integrating the PSD over the frequency band that defines the tone. SPLs are compared in Table 3 and Fig. 22a, indicating that the fully-correlated assumption is inaccurate.

Assuming that the resonators are completely decorrelated leads to a reduction in PSD for both tones in the 2R case, but only for the fundamental tone in the 1R case. This can be attributed to phase cancellation occurring in the one-resonator case for the fundamental tone, stemming from the different source-to-observer distances for the various observer locations.

The SPLs of the fundamental and the second harmonic for the 1R case are compared with the measurements in Table 3 and in Fig. 22a. The predicted results are shown as mean values with error bars, where the mean value is the average of the two SPLs obtained using the completely correlated

1 and the completely uncorrelated assumptions, and the error bar is the difference between the two.  
 2 The predicted results have been corrected for atmospheric absorption; the corrections are given in  
 3 Table 3. Figure 22a suggests that the resonators in the deterrent are partially correlated. Figure 22b  
 4 shows the predicted SPL directivity patterns for the fundamental and the second harmonic. The  
 5 deterrent is only on the suction side in the simulations. Hence, the radiation intensity is high ahead  
 of and above the blade.

Table 3: Sound pressure level (SPL wref  $20\mu\text{pa}$ ) values for the fundamental and the second harmonic for the HF deterrent and atmospheric attenuation at those frequencies. Predictions are made using two assumptions: full correlation across the resonators and zero correlation across the resonators for the 1R case. Tonal SPL values are obtained by integrating the pressure PSD spectra over frequency bands around the tones.

<i>Frequency</i> [kHz]	<i>Experiment</i> [dB]	<i>Prediction</i> [dB]				<i>Atm. abs.</i> [dB/m]
		<i>Correlated</i>	<i>Uncorrelated</i>	<i>Mean</i>	<i>Error</i>	
20.5	78.98	98.37	63.72	81.05	$\pm 17.33$	0.55
41.0	72.77	70.12	70.14	70.13	$\pm 0.01$	1.36

6

## 7 6. Conclusions

8 This paper introduces a novel, passive, blade-mounted bat deterrent for wind turbines and  
 9 presents a comprehensive computational and experimental investigation of its acoustic character-  
 10 istics and impact on the blade’s aerodynamic performance. The deterrent is based on the concept  
 11 of aerodynamic whistles. It uses resonating cavities that are placed near the leading edge of the  
 12 blade. Two designs are considered: a low-frequency deterrent (LF) and a high-frequency deter-  
 13 rent (HF). The HF deterrent is a geometrically scaled-down version of the LF deterrent. The  
 14 Helmholtz resonance frequencies of the LF and HF deterrents are approximately 10 kHz and 20.5  
 15 kHz respectively.

16 The experiments were conducted in the Virginia Tech Stability Wind Tunnel where acoustic  
 17 measurements were made with an acoustic array mounted on the Starboard side wall of the tunnel.  
 18 In line with the existing literature on cavity noise, the measurements indicate that there is a  
 19 minimum flow speed ( $V_{\infty, \text{min}}$ ) below which the deterrents do not produce sound.  $V_{\infty, \text{min}}$  is a  
 20 function of the deterrent geometry; it lies between 55 and 60 m/s for the HF deterrent and between

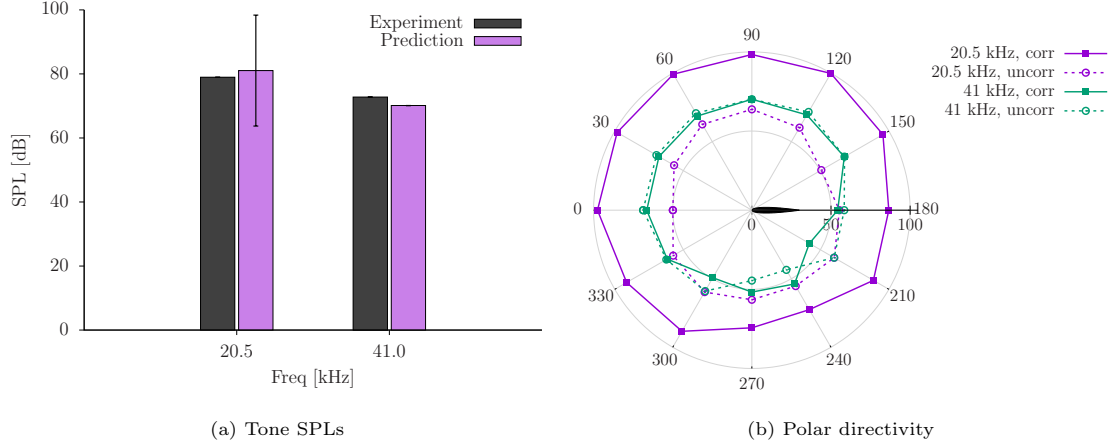


Figure 22: Numerical predictions of the farfield (1 m) sound pressure levels (SPLs) of the fundamental (20.5 kHz) and the second harmonic (41 kHz) corrected for atmospheric absorption. The SPLs are obtained by integrating the PSD spectra over a frequency band (2 kHz for simulations and 1.6 kHz for experiments) around each tone. (a) SPL comparison for the fundamental tone and the second harmonic at 90° polar angle between measurements and numerical prediction for the HF deterrent (one-resonator configuration) at  $V_\infty = 60$  m/s and  $\alpha = 0^\circ$ . The predicted SPLs are the average of the results obtained by assuming full correlation and zero correlation across the resonators; the error bar denotes the difference between the two. (b) Predicted directivity patterns assuming the resonators are completely correlated (solid) and completely uncorrelated (dashed).

1 30 and 35 m/s for the LF deterrent. The peak radiation frequency and the radiated acoustic  
 2 intensity increase slightly with  $V_\infty$ . A small increase in radiated acoustic intensity is also observed  
 3 with blade angle of attack ( $\alpha$ ) due to the increase in local flow speed over the deterrent.

4 Numerical simulations are performed in two and three dimensions using the uRANS model. The  
 5 simulations confirm the presence of a deterrent-specific onset flow speed and also reveal that there  
 6 is a  $V_{\infty, \max}$  beyond which resonance does not take place. The peak frequency increases linearly  
 7 with  $V_\infty$ , which aligns with the theoretical estimate of the first Rossiter mode frequency. A slight  
 8 increase in peak frequency is also observed with  $\alpha$ . The predicted trends with  $V_\infty$  and  $\alpha$  agree  
 9 with the measurements. Three-dimensional simulations are performed to quantitatively compare  
 10 the predictions with the experiments. Two configurations are considered - one modeling a single  
 11 resonator and the other modeling two resonators, both with spanwise periodic boundaries. The  
 12 results show that the unsteady pressures in the resonators of the two-resonator configuration are  
 13 nearly out of phase, with each resonator exhibiting significantly higher unsteadiness than the one-

1 resonator configuration. The out-of-phase behavior, however, leads to partial cancellation of the  
2 odd harmonics in the radiated sound.

3 Acoustic propagation is performed by solving the Ffowcs Williams and Hawkings equation. The  
4 one-resonator configuration is used for farfield prediction. Since the simulations use a smaller span  
5 than the deterrents used in the experiments, two sets of farfield predictions are made with the  
6 following assumptions regarding the degree of correlation between the resonators: (1) 100% corre-  
7 lation and (2) 0% correlation. The tonal SPLs predicted using these two methods are expected to  
8 bound the measured values. The overall agreement with the measured data is modest. Tonal direc-  
9 tivity shows the highest intensity directly upstream of the blade and the lowest on the downstream  
10 pressure side.

## 11 **Acknowledgments**

12 This material is based upon work supported by the U.S. Department of Energy’s Office of  
13 Energy Efficiency and Renewable Energy (EERE) under the Wind Energy Technologies Office  
14 Award Number DE-EE0008731 and DE-EE0011086. The National Science Foundation (Grants  
15 CBET-1554196 and 1935255) also partially supported this research. We also acknowledge the  
16 computational resources provided by the Department of Defense through the US Air Force Office  
17 of Scientific Research (Award # FA9550-23-1-0016) and the Iowa State University.

## **References**

- Arnett, E.B., Baerwald, E.F., 2013. Impacts of wind energy development on bats: implications for conservation, in: *Bat evolution, ecology, and conservation*. Springer, pp. 435–456.
- Arnett, E.B., Hein, C.D., Schirmacher, M.R., Huso, M.M., Szewczak, J.M., 2013. Evaluating the effectiveness of an ultrasonic acoustic deterrent for reducing bat fatalities at wind turbines. *PloS one* 8.
- Baerwald, E.F., Edworthy, J., Holder, M., Barclay, R.M., 2009. A large-scale mitigation experiment to reduce bat fatalities at wind energy facilities. *The Journal of Wildlife Management* 73, 1077–1081.



- Bass, H.E., Sutherland, L.C., Zuckerwar, A.J., Blackstock, D.T., Hester, D., 1995. Atmospheric absorption of sound: Further developments. *The Journal of the Acoustical Society of America* 97, 680–683.
- Bennett, G.J., Stephens, D.B., Rodriguez Verdugo, F., 2017. Resonant mode characterisation of a cylindrical helmholtz cavity excited by a shear layer. *The Journal of the Acoustical Society of America* 141, 7–18.
- Chanaud, R.C., 1970. Aerodynamic whistles. *Scientific American* 222, 40–47.
- Chen, L., Harding, C., Sharma, A., MacDonald, E., 2016. Modeling noise and lease soft costs improves wind farm design and cost-of-energy predictions. *Renewable Energy* 97, 849–859.
- Cheng, T.L., Reichard, J.D., Coleman, J.T., Weller, T.J., Thogmartin, W.E., Reichert, B.E., Bennett, A.B., Broders, H.G., Campbell, J., Etchison, K., et al., 2021. The scope and severity of white-nose syndrome on hibernating bats in north america. *Conservation Biology* 35, 1586–1597.
- Covert, E.E., 1970. An approximate calculation of the onset velocity of cavity oscillations. *AIAA journal* 8, 2189–2194.
- Cryan, P.M., 2011. Wind turbines as landscape impediments to the migratory connectivity of bats. *Environmental Law* , 355–370.
- Cryan, P.M., Brown, A.C., 2007. Migration of bats past a remote island offers clues toward the problem of bat fatalities at wind turbines. *Biological conservation* 139, 1–11.
- Drela, M., 1989. Xfoil: An analysis and design system for low reynolds number airfoils, in: *Low Reynolds Number Aerodynamics: Proceedings of the Conference Notre Dame, Indiana, USA, 5–7 June 1989*, Springer. pp. 1–12.
- Dykes, K., Resor, B., Platt, A., Guo, Y., Ning, A., King, R., Parsons, T., Petch, D., Veers, P., 2014. Effect of tip-speed constraints on the optimized design of a wind turbine. Technical Report NREL/TP-5000-61726. National Renewable Energy Lab.(NREL), Golden, CO (United States).
- Frick, W.F., Kingston, T., Flanders, J., 2020. A review of the major threats and challenges to global bat conservation. *Annals of the New York Academy of Sciences* 1469, 5–25.

- Friedenberg, N.A., Frick, W.F., 2021. Assessing fatality minimization for hoary bats amid continued wind energy development. *Biological Conservation* 262, 109309.
- Gharib, M., Roshko, A., 1987. The effect of flow oscillations on cavity drag. *Journal of Fluid Mechanics* 177, 501–530.
- Gloerfelt, X., 2009. Cavity noise. VKI lecture series 3.
- Good, R.E., Iskali, G., Lombardi, J., McDonald, T., Dubridge, K., Azeka, M., Tredennick, A., 2022. Curtailment and acoustic deterrents reduce bat mortality at wind farms. *The Journal of Wildlife Management* , e22244.
- Gorresen, P.M., Cryan, P.M., Dalton, D.C., Wolf, S., Johnson, J.A., Todd, C.M., Bonaccorso, F.J., 2015. Dim ultraviolet light as a means of deterring activity by the hawaiian hoary bat *lasiurus cinereus semotus*. *Endangered Species Research* 28, 249–257.
- Hayes, M.A., 2013. Bats Killed in Large Numbers at United States Wind Energy Facilities. *Bio-Science* 63, 975–979. URL: <https://doi.org/10.1525/bio.2013.63.12.10>, doi:10.1525/bio.2013.63.12.10.
- Horn, J.W., Arnett, E.B., Jensen, M., Kunz, T.H., 2008a. Testing the effectiveness of an experimental acoustic bat deterrent at the maple ridge wind farm. Report Prepared for: The Bats and Wind Energy Cooperative and Bat Conservation International, Austin, TX .
- Horn, J.W., Arnett, E.B., Kunz, T.H., 2008b. Behavioral responses of bats to operating wind turbines. *The Journal of Wildlife Management* 72, 123–132.
- Hu, H., Wang, Z., Ozbay, A., Tian, W., Sharma, A., 2015. An experimental investigation on the wake characteristics behind a novel twin-rotor wind turbine, in: 33rd Wind Energy Symposium, p. 1663.
- Huzzen, B., 2019. Does a Textured Coating Alter Bat Activity and Behavior in Proximity to Wind Turbine Towers? Ph.D. thesis. Texas Christian University.
- ISO 9613-1:1996, 1995. Calculation of the Absorption of Sound by the Atmosphere. Standard. International Organization for Standardization.

- Krishnamurty, K., 1955. Acoustic radiation from two-dimensional rectangular cutouts in aerodynamic surfaces. Technical Report TN 3487. National Advisory Committee for Aeronautics.
- Kunz, T.H., Arnett, E.B., Erickson, W.P., Hoar, A.R., Johnson, G.D., Larkin, R.P., Strickland, M.D., Thresher, R.W., Tuttle, M.D., 2007. Ecological impacts of wind energy development on bats: questions, research needs, and hypotheses. *Frontiers in Ecology and the Environment* 5, 315–324.
- Martin, C.M., Arnett, E.B., Stevens, R.D., Wallace, M.C., 2017. Reducing bat fatalities at wind facilities while improving the economic efficiency of operational mitigation. *Journal of Mammalogy* 98, 378–385.
- Menter, F.R., 1994. Two-equation eddy-viscosity turbulence models for engineering applications. *AIAA journal* 32, 1598–1605.
- Moghadassian, B., Rosenberg, A., Sharma, A., 2016. Numerical investigation of aerodynamic performance and loads of a novel dual rotor wind turbine. *Energies* 9, 571.
- Moghadassian, B., Sharma, A., 2018. Inverse design of single-and multi-rotor horizontal axis wind turbine blades using computational fluid dynamics. *Journal of Solar Energy Engineering* 140.
- Moghadassian, B., Sharma, A., 2020. Designing wind turbine rotor blades to enhance energy capture in turbine arrays. *Renewable Energy* 148, 651–664.
- Mongeau, L., Brown, D., Kook, H., Zorea, S., 1997. A predictive model for the interior pressure oscillations from flow over vehicle openings. *SAE transactions* , 2675–2684.
- O’Shea, T.J., Cryan, P.M., Hayman, D.T., Plowright, R.K., Streicker, D.G., 2016. Multiple mortality events in bats: a global review. *Mammal review* 46, 175–190.
- Rayleigh, J.W.S.B., 1896. *The theory of sound*. volume 2. Macmillan.
- Romano, W.B., Skalski, J.R., Townsend, R.L., Kinzie, K.W., Coppinger, K.D., Miller, M.F., 2019. Evaluation of an acoustic deterrent to reduce bat mortalities at an illinois wind farm. *Wildlife Society Bulletin* 43, 608–618.
- Rosenberg, A., Selvaraj, S., Sharma, A., 2014. A novel dual-rotor turbine for increased wind energy capture. *Journal of Physics: Conference Series* 524, 012078.

- Rosenberg, A., Sharma, A., 2016. A prescribed-wake vortex lattice method for preliminary design of co-axial, dual-rotor wind turbines. *Journal of Solar Energy Engineering* 138.
- Rossiter, J., 1966. Wind-tunnel experiments on the flow over rectangular cavities at subsonic and transonic speeds. Technical Report R & M No. 3438. Aeronautical Research Council, Ministry of Aviation.
- Sarohia, V., 1975. Experimental and Analytical Investigation of Oscillations in Flows over Cavities. Ph.D. thesis. California Institute of Technology.
- Schirmacher, M.R., 2020. Evaluating the effectiveness of an ultrasonic acoustic deterrent in reducing bat fatalities at wind energy facilities. Technical Report. Bat Conservation International, Austin, TX (United States).
- Sharma, A., Zeng, Z., 2023. Passive Ultrasonic Deterrents to Reduce Bat Mortality in Wind Farms. Technical Report. Department of Energy.
- Smallwood, K.S., 2013. Comparing bird and bat fatality-rate estimates among north american wind-energy projects. *Wildlife Society Bulletin* 37, 19–33.
- Szoke, M., Borgoltz, A., Kuester, M., Intaratep, N., Ravetta, P., 2022. Design and in-situ calibration of a beamforming array for high-frequency noise measurements in a hybrid-anechoic wind tunnel, in: 28th AIAA/CEAS Aeroacoustics Conference, p. 132.
- Voigt, C.C., Lehnert, L.S., Petersons, G., Adorf, F., Bach, L., 2015. Wildlife and renewable energy: German politics cross migratory bats. *European Journal of Wildlife Research* 61, 213–219.
- Weaver, S.P., Hein, C.D., Simpson, T.R., Evans, J.W., Castro-Arellano, I., 2020. Ultrasonic acoustic deterrents significantly reduce bat fatalities at wind turbines. *Global Ecology and Conservation* 24, e01099.
- Wilson, T., Beavers, G., DeCoster, M., Holger, D., Regenfuss, M., 1971. Experiments on the fluid mechanics of whistling. *The Journal of the Acoustical Society of America* 50, 366–372.
- Wu, X., Sharma, A., 2020. Artefacts of finite span in vortex-induced vibration simulations. *Applied Ocean Research* 101, 102265.

Zeng, Z., Sharma, A., 2021. Experimental and numerical aeroacoustic analysis of an ultrasound whistle, in: AIAA Aviation Forum, Washington DC, USA.

Zeng, Z., Sharma, A., 2023. Aerodynamic-whistles-based ultrasonic tone generators for bat deterrence. *Physics of Fluids* 35.

Zeng, Z., Sharma, A., 2025. Frequency modulation of an aerodynamic whistle-based bat deterrent. *Applied Acoustics* 228, 110276.

Zimmerman, R., 2009. Biologists struggle to solve bat deaths. *Science* 324, 1134–1135. doi:[10.1126/science.324\\\_1134](https://doi.org/10.1126/science.324\_1134).

## Appendices

### 1 A. Standing waves in the Stability Wind Tunnel

2 The measured spectra in the Stability Wind Tunnel show several sharp peaks above the broad  
3 peaks at the frequencies corresponding to the resonance frequencies of the whistle/deterrent (see the  
4 gray curve in Fig. 23). A Gaussian filter is applied to the signal to reveal the spectrally broadened  
5 peaks that can be expected due to slight geometric differences between the resonators in a deterrent,  
6 each resonator having a slightly different resonance frequency.

7 We hypothesize that these additional sharp peaks are due to standing waves/modes trapped  
8 between the blade model and the hard sidewall of the tunnel on which the beamforming array is  
9 mounted. Figure 24 illustrates this phenomenon. The channel between the blade and the hard  
10 sidewall can act as a waveguide, amplifying the acoustic modes supported by the hard-wall bound-  
11 ary conditions. Assuming hard-wall boundary conditions at both ends (blade surface and tunnel  
12 sidewall) and ignoring the blade thickness, the expected frequency gap,  $\Delta f$ , between these tones  
13 is approximately 185 Hz assuming the speed of sound,  $c_0 = 340$  m/s. The measured data shows  
14 frequency shifts that are integer multiples of this  $\Delta f$ , suggesting that multiple modes ( $n = 1, 2, \dots$ )  
15 are excited.

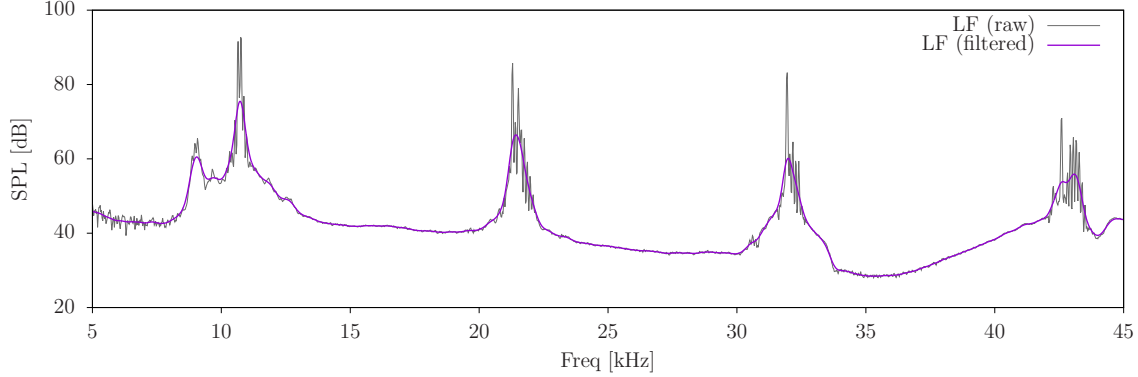


Figure 23: Integrated beamforming sound pressure level (SPL) spectra. The raw signal (gray) shows multiple sharp peaks around each expected tone; the Gaussian-filtered signal (purple) shows the expected spectral broadening of tones due to differences in the geometry of the resonators.

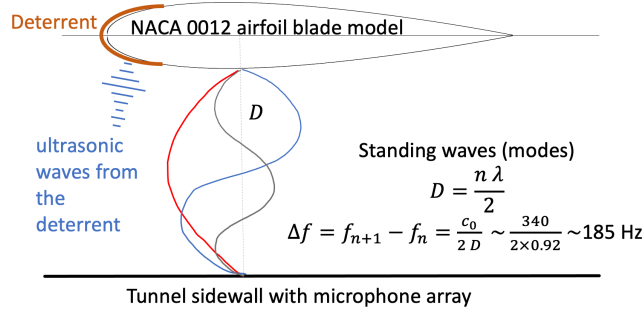


Figure 24: An illustration of standing waves between the airfoil/blade model and the hard sidewall of the tunnel on which the microphone array is installed.

## 1 B. Beamform maps for the HF deterrent

2 The imprecise determination of source locations in the beamform maps shown in Figs. 9 and 10  
 3 is investigated further through simulation. We note that the tightly spaced resonators could have  
 4 coupled end conditions at their openings, which establish a fixed phase condition between the tonal  
 5 pressure sources. The effect of this coupling on the beamform maps is investigated by simulating  
 6 a distribution of monopole sources similar to the LF and HF deterrents with in-phase and out-of-  
 7 phase resonance of adjacent sources. The coordinate system is such that the simulated sources are  
 8 distributed in the vertical direction about  $x = y = 0$ . Each monopole source is located at the center  
 9 of each resonator from the experimental measurements extending from  $y = -0.1346$  m to 0.1346

1 m. The relative locations of the microphones are matched to the positions in the measurement.

2 Two frequencies are analyzed. The beamform maps produced by simulation of the LF deterrent

3 at a resonant frequency of 10.6 kHz are shown in Fig. 25. Similarly, results for the HF deterrent

4 at a resonant frequency of 23.6 kHz are shown in Fig. 26. For both deterrents, the map shows a

5 single peak at the center of the deterrent locations if all resonators are assumed to be in phase.

6 When adjacent resonators are 180° out-of-phase, the source distribution becomes more complex.

7 For the LF deterrent, peaks appear near the bottom and top of the deterrent location. The HF

8 deterrent produces a beamform map with strong scattered sidelobes that is not a reflection of

9 the correct source distribution. The results shown in the out-of-phase calculations are similar

10 to the experimental results. Although the true phase between resonators for both deterrents in

11 the experimental measurements is unknown and most likely lies between these two extremes, this

12 analysis suggests that the phase between the distributed tonal sources can produce the ambiguous

13 beamform maps presented in Figs. 9 and 10.

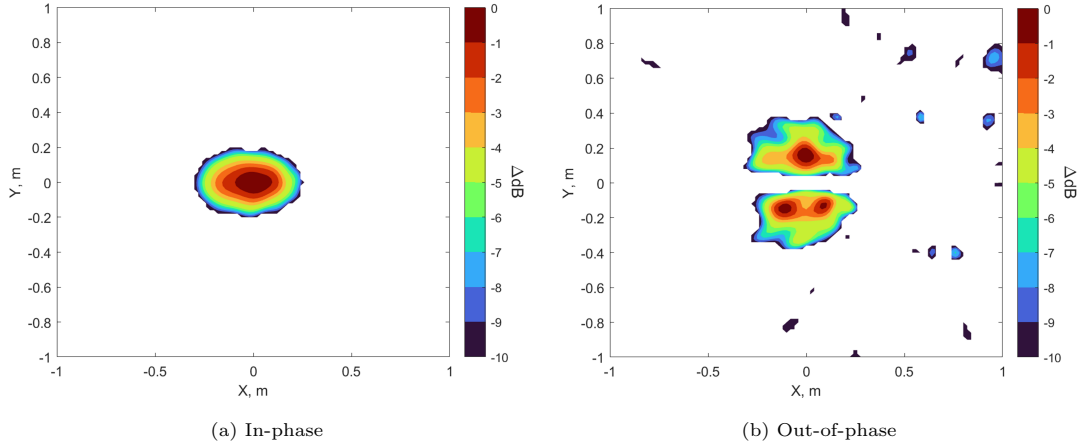


Figure 25: Simulated beamform maps of the LF deterrent at 10.6 kHz with adjacent resonators a) in-phase b) and 180° out-of-phase.

### 14 C. Mesh sensitivity study

15 A study on spatial and temporal mesh refinement was conducted for the two-dimensional con-

16 figuration. Favorable comparisons with XFOIL (Fig. 12) confirmed the accuracy of the boundary

17 layer flow simulation over the airfoil using the baseline mesh. Consequently, only the mesh in and

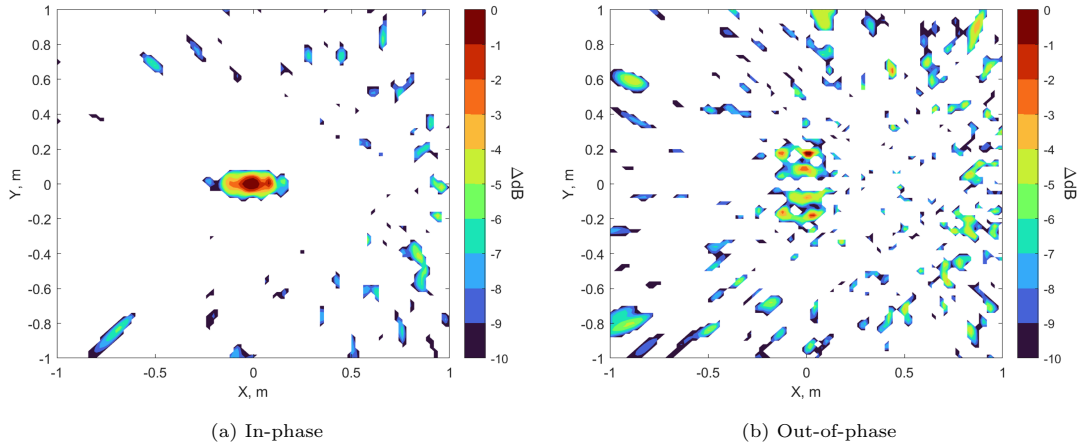


Figure 26: Simulated beamform maps of the HF deterrent at 23.6 kHz with adjacent resonators a) in-phase b) and 180° out-of-phase.

1 around the resonator was modified to ensure mesh independence in the acoustic results. Four mesh  
 2 types were created – Coarse, Baseline, Fine, and Finest – and two time step sizes were evaluated  
 3 for the baseline mesh (see Table 4). As shown in Fig. 27, the pressure power pred at the center  
 4 of the resonator is nearly independent of mesh size beyond the baseline mesh, and a time step of  
 5  $\Delta t = 2.5E - 07$  is sufficient. The findings of the study are summarized in Fig. 27.

Table 4: Test cases for mesh refinement study.  $\Delta x_{\text{base}}$  is the approximate mesh size (estimated as cube-root of cell volume) in the resonator.

<i>Name</i>	$\Delta x / \Delta x_{\text{base}}$	$\Delta t$ (in s)
Coarse	1.50	2E-07
Baseline	1.00	2.5E-07, 5.0E-07
Fine	0.75	2.5E-07
Finest	0.50	2.5E-07

#### 6 D. Noise prediction using small-span simulations

7 Computational cost increases proportionately with domain size in fluid flow simulations. Span  
 8 periodicity is typically employed to reduce the domain size. If there is physical periodicity in



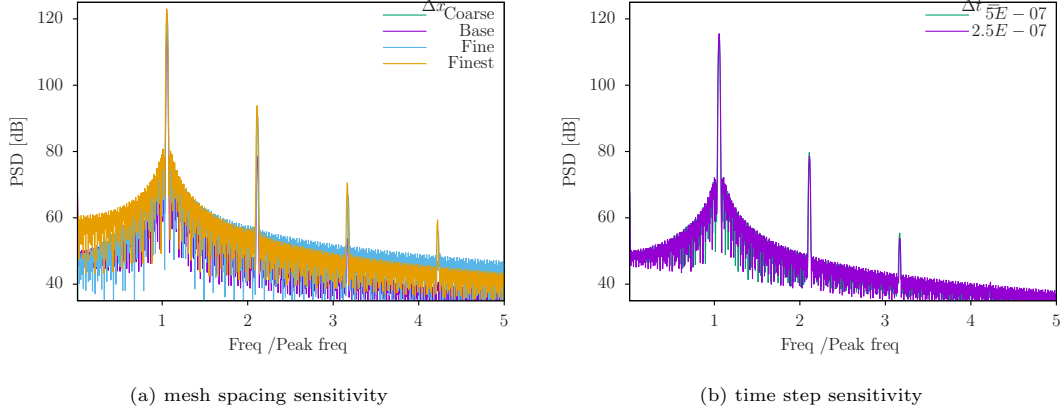


Figure 27: Results from a mesh refinement study: (a) mesh spacing,  $\Delta x$ , and (b) time step,  $\Delta t$ . The power spectral density spectra correspond to the unsteady pressure at the center of the resonator.

1 the span direction, and the full span is simulated, then the boundary condition replicates reality.  
 2 Otherwise, the numerically imposed periodicity introduces some artifacts in the solution (Wu and  
 3 Sharma, 2020). Depending on the spanwise coherence of the problem, these artifacts can be negli-  
 4 gible. Consider the schematic in Fig. 28 where  $B$  is the computational model with a span of  $\Delta x$ ,  
 5 which is a third of the span of the physical model made up of blocks  $A$ ,  $B$ , and  $C$ . Say our interest  
 6 is computing the noise from the physical model at observer location  $b$ . Denote the radiated acoustic  
 7 pressure from block  $B$  at observer location  $b$  by  $p_{B \rightarrow b}$ . Similarly, the radiated acoustic pressure  
 8 from  $A$  to  $b$  and  $C$  to  $b$  are  $p_{A \rightarrow b}$  and  $p_{C \rightarrow b}$  respectively.

9 The numerical model uses spanwise periodicity. Hence, in the numerical solution,  $A$  and  $C$  are  
 10 replicas of  $B$ . If the sources in  $A$ ,  $B$ , and  $C$  are fully correlated, then the noise at observer  $b$  from  
 11 the full physical model is

$$p_b = p_{A \rightarrow b} + p_{B \rightarrow b} + p_{C \rightarrow b}. \quad (8)$$

12 If the sources are totally uncorrelated, then

$$p_b^2 = p_{A \rightarrow b}^2 + p_{B \rightarrow b}^2 + p_{C \rightarrow b}^2. \quad (9)$$

13 Because of the relative distances and the radiation angles involved, and the fact that the nu-  
 14 merical solution in  $A$ ,  $B$ , and  $C$  are identical,  $p_{A \rightarrow b}$  is identical to  $p_{B \rightarrow c}$ , and  $p_{C \rightarrow b}$  is identical to

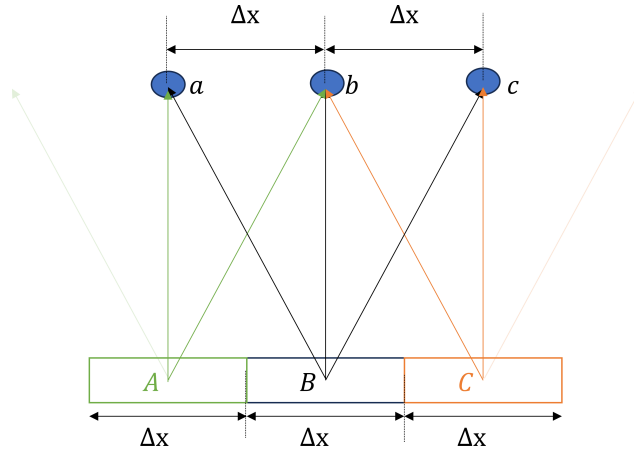


Figure 28: A schematic to explain how a small-span-deterrent simulation result is used to predict noise from the full-scale deterrent.

1  $p_{B \rightarrow a}$ . These relations can be used with Eqs. 8 and 9 to write

$$\begin{aligned}
 p_b &= p_{B \rightarrow c} + p_{B \rightarrow b} + p_{B \rightarrow a}, & (\text{completely correlated}) \\
 p_b^2 &= p_{B \rightarrow c}^2 + p_{B \rightarrow b}^2 + p_{B \rightarrow a}^2 & (\text{completely uncorrelated}).
 \end{aligned} \tag{10}$$

Equation 10 shows that the noise from the full physical model at observer  $b$  can be obtained by appropriately adding the noise from the simulation of a smaller model ( $B$ ) at multiple observer locations ( $a$ ,  $b$ , and  $c$ ) that are spaced the model span length ( $\Delta x$ ) apart. The example here uses three blocks but can be extended to an arbitrary number of blocks. The spanwise periodicity assumption is invalid if the sources are partially correlated. However, one can approximate that the actual noise would lie between the two predictions obtained assuming zero and full correlation.